Experimental techniques for turbulent Taylor–Couette flow and Rayleigh–Bénard convection

Invited Article

Experimental techniques for turbulent Taylor–Couette flow and Rayleigh–Bénard convection

Chao Sun[1] and Quan Zhou[2]

[1] Physics of Fluids Group, Faculty of Science and Technology, J M Burgers Centre for Fluid Dynamics, University of Twente, The Netherlands
[2] Shanghai Institute of Applied Mathematics and Mechanics, Shanghai University, Shanghai 200072, People's Republic of China

E-mail: c.sun@utwente.nl and qzhou@shu.edu.cn

Abstract

Taylor–Couette (TC) flow and Rayleigh–Bénard (RB) convection are two systems in hydrodynamics, which have been widely used to investigate the primary instabilities, pattern formation, and transitions from laminar to turbulent flow. These two systems are known to have an elegant mathematical similarity. Both TC and RB flows are closed systems, i.e. the total energy dissipation rate exactly follows from the global energy balances. From an experimental point of view, the inherent simple geometry and symmetry in these two systems permits the construction of high precision experimental setups. These systems allow for quantitative measurements of many different variables, and provide a rich source of data to test theories and numerical simulations. We review the various experimental techniques in these two systems in fully developed turbulent states.

Keywords: turbulence, Taylor–Couette flow, Rayleigh–Bénard flow
Mathematics Subject Classification: 76F10, 76F25, 76F35, 76F40, 76U05

(Some figures may appear in colour only in the online journal)

1. Introduction to the types of flow

1.1. Turbulent Taylor–Couette flow

Taylor–Couette (TC) flow systems consist of a working fluid confined between two coaxial, differentially rotating cylinders (inner cylinder—IC and outer cylinder—OC) with radii r_i and r_o. The cylinders are able to rotate independently from each other with an angular rotation rate of ω_i for the IC and ω_o for the OC. The relative rotation of the cylinders can be in either the co-rotating or counter-rotating direction. The volume between cylinders is enclosed by two
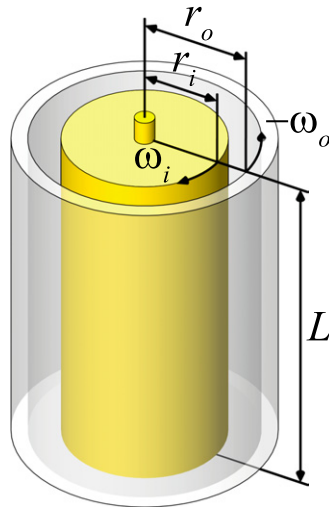
Figure 1. A schematic of a TC apparatus. Two concentric cylinders can rotate independently. The rotation rates of the IC and OC are ω_i and ω_o, and the radii are r_i and r_o. The gap is defined as the volume where the working fluid is, which has gap-size $r_o - r_i$, and height L.

parallel lids with a distance 'L' between them. See figure 1 for a schematic illustration of a TC apparatus.

The TC is most conveniently described in a cylindrical coordinate system (r, ϕ, z) between the IC radius r_i and the OC radius r_o. The aspect ratio is given by $\Gamma = L/d$, where L is the cell height and the gap width is $d = r_o - r_i$. Here we choose the control parameters in the TC system as the Taylor number (Ta), the ratio of the angular velocities (a) and the radius ratio (η) which are defined as follows:

$$Ta = \tfrac{1}{4}\sigma(r_o - r_i)^2(r_i + r_o)^2(\omega_i - \omega_o)^2 \nu^{-2}, \tag{1}$$

$$a = -\omega_o/\omega_i, \tag{2}$$

$$\eta = r_i/r_o. \tag{3}$$

In general, we define the angular velocity of the IC ω_i as positive, whereas the angular velocity of the OC ω_o is either positive (co-rotation, $a < 0$) or negative (counter-rotation, $a > 0$). The dimensionless control parameters (Ta, a) of the system can also be expressed in terms of the IC and OC Reynolds numbers

$$Re_i = r_i\omega_i d/\nu \tag{4}$$

$$Re_o = r_o\omega_o d/\nu, \tag{5}$$

where ν is the kinematic viscosity.

One of the response parameters is the degree of turbulence of the flow in the gap of the cylinders—i.e. quantified by the wind Reynolds number of the flow, which measures the amplitudes or fluctuations of the r- and z-components of the velocity field (u_r and u_z). Since the time-averaged wind velocity is generally zero—i.e. $\langle u_r \rangle \simeq 0$ and $\langle u_\phi \rangle \simeq 0$ for only IC rotation, the standard deviation of the wind velocity is mostly used to quantify the wind Reynolds number:

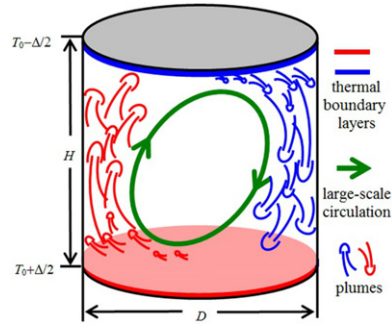$$Re_w = \frac{\sigma_{u_w}(r_o - r_i)}{\nu}. \tag{6}$$

Figure 2. A sketch of Rayleigh–Bénard convection in a cylindrical cell with unit aspect ratio. The red-shaded areas of the cell show regions with hot fluid, while the blue areas indicate cold fluid. The arrows give the direction of the LSC.

$\sigma_{u_{\mathrm{w}}}$ could be chosen to be the standard deviation of either the radial or axial velocity. Here we mostly use the radial velocity component.

Another response parameter is the torque τ to maintain the rotation of the IC at a constant angular velocity. The dimensionless form of the torque is defined as

$$G = \frac{\tau}{2\pi \ell \rho_{\mathrm{fluid}} \nu^2},\tag{7}$$

where ρ_{fluid} is the density of the fluid and ℓ the height of the cylinder. Another frequently used parameter to represent the data is the friction coefficient on the IC $c_{\mathrm{f}} = ((1-\eta)^2/\pi)G/Re_{\mathrm{i}}^2$ [1].

Based on the analogy between TC and Rayleigh–Bénard (RB), Eckhardt, Grossmann and Lohse (hereafter referred to as EGL) [2] defined a non-dimensionalized transport quantity as Nu_ω 'Nusselt number' in terms of the laminar transport,

$$Nu_\omega = \frac{\tau}{2\pi L \rho_{\mathrm{fluid}} J_{\mathrm{lam}}^\omega},\tag{8}$$

where $J_{\mathrm{lam}}^\omega = 2\nu r_{\mathrm{i}}^2 r_{\mathrm{o}}^2 (\omega_{\mathrm{i}} - \omega_{\mathrm{o}})/(r_{\mathrm{o}}^2 - r_{\mathrm{i}}^2)$ is the conserved angular velocity flux in the laminar case. With this choice of control and response parameters, EGL derived a close analogy between turbulent TC and turbulent RB flow, building on the Grossmann and Lohse (GL) theory for RB flow [3–5].

With respect to flow instabilities, flow transitions, and pattern formation, TC flow is well-explored, and it displays a surprisingly large variety of flow states beyond the onset of instabilities [6–12]. Here we focus on TC flow in fully developed turbulent states. The parameters Ta and Nu_ω in the TC system are analogous to Ra and Nu in RB flow (to be discussed below). In the TC flow, one would like to characterize the flow structures, and measure the variables such as the angular velocity of the flow (transport quantity), the radial velocity (wind velocity), the global torque, and the local turbulent angular velocity flux.

1.2. Turbulent RB convection

The typical RB system consists of a working fluid confined between a cold top and a warm bottom plate [13–15]. As shown in figure 2, once the convective thermal turbulence has been well developed in the system, two types of boundary layers coexist near the top and bottom plates: one kinematic boundary layer and one thermal boundary layer. Thermal structures, like plumes, are generated and detached from the boundary layers, and then move into the bulk fluid under the effects of the buoyancy. During the rising and falling of thermal plumes,

the self-organization of the plume motion will result in a large-scale mean flow of the system, i.e. the large-scale circulation (LSC). The convective motion dramatically enhances the heat transport through the fluid layer, and understanding its nature is of fundamental interest and of great importance in the study of turbulent RB systems. The global heat transport is usually measured in terms of the Nusselt number Nu, defined as:

$$Nu = \frac{J}{\lambda_{\mathrm{f}} \Delta / H},$$ (9)

where J is the heat-current density across a fluid layer of thermal conductivity λ_{f} with height H and with an applied temperature difference Δ.

The dynamics of the system depends on the turbulent intensity and the fluid properties. These are characterized, respectively, by the Rayleigh number Ra and the Prandtl number Pr, defined as

$$Ra = \frac{\alpha g H^3 \Delta}{\nu \kappa} \qquad \text{and} \qquad Pr = \frac{\nu}{\kappa},$$ (10)

where g is the acceleration due to gravity, and α, ν and κ are the thermal expansion coefficient, kinematic viscosity, and thermal diffusivity of the convecting fluid respectively, for which the Oberbeck–Boussinesq approximation is considered as valid, i.e. the fluid density ρ_{fluid} is assumed to depend linearly on the temperature T, $\rho_{\mathrm{fluid}} = \rho_0[1 - \beta(T - T_0)]$, with ρ_0 and T_0 being reference values. In any laboratory experiments, a lateral sidewall is indispensable, so a third control parameter, the aspect ratio Γ, enters the problem. It is defined as the lateral confinement over the cell height. For a cylindrical cell (as shown in figure 2) $\Gamma \equiv D/H$, where D is the diameter of the cell.

In the RB flow, one would like to characterize the flow structures, and measure the variables such as the temperature and velocity of the fluid particles, and global and local heat flux.

2. Experiments in turbulent TC system

2.1. Flow visualization—turbulent flow structures

Flow visualization techniques are particularly useful in studying hydrodynamic systems which form spatial patterns due to secondary flows, for example Taylor vortices in TC flow [16]. There are many flow visualization techniques available, and here we only discuss the techniques which use anisotropic particles and small bubbles.

Matisse and Gorman [16] have described the flow visualization technique using anisotropic particles. The idea is to use particles dispersed in the working fluids to reflect the flow structures. Anisotropic particles are desirable to be used as they align themselves with the flow. Kalliroscope flakes are widely used for this purpose. Generally, Kalliroscope flakes are made from guanine, with a size of a few micrometres and a density of around $1.62 \, \mathrm{g \, cm^{-3}}$ [16]. In order to use this method, it is desirable to match the density of the flakes to the working fluid to reduce the sedimentation effect of the flakes. This visualization method has been widely used in the TC community to study the flow instability, pattern formation, chaos, and transition to turbulence (see e.g. [7, 8, 17, 18]).

Here, we show an example of the flow visualization using Kalliroscope flakes in the Twente turbulent Taylor–Couette (T^{3}C) facility. A detailed description of the T^{3}C system can be found in [20]. The IC has a radius of 20.0 cm and the OC radius is 27.9 cm. The 7.9 cm gap is vertically confined by the top and bottom plates with a distance of 92.7 cm. The experimental setup for the flow visualization is shown in figure 3(a). The fluid inside the TC gap is seeded with the reflective flakes and illuminated by a laser sheet. A high-speed camera is aligned
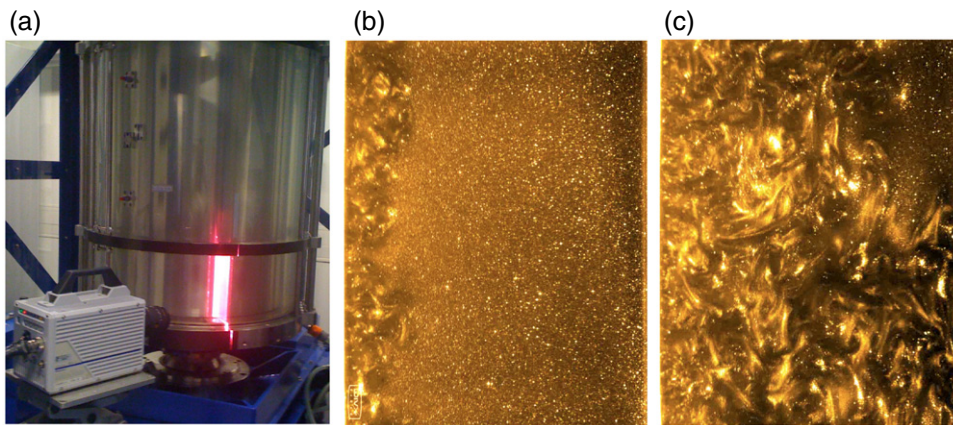
(a)   (b)   (c)

Figure 3. Figure reproduced from [19]. (*a*) A photograph of the experimental setup for flow visualization in the T³C system. The flow is seeded with reflective Kalliroscope flakes and illuminated by a laser sheet. (*b*), (*c*) High-speed imaging snapshots show the evolution of the turbulent structures when the IC starts to rotate. On the left side is the IC wall, and on the right side is the OC wall. The distortion due to the curved surface is not corrected for these snapshots.

perpendicular to the light sheet to image the reflected light from the flakes. In this experiment, the OC is stationary, and the IC starts to rotate. As shown in figures 3(*b*) and (*c*), the recordings reveal the turbulent structures that emerge from the IC and their eventual penetration to fill the entire fluid layer.

It has been found that inertial particles in turbulence do not fully follow the fluid motion and distribute inhomogeneously within the turbulent flow, leading to clustering or preferential concentration [21, 22]. Light particles tend to cluster in high vorticity regions of the turbulent flow [23]. One can take advantage of this property of the light particles to visualize the structures of turbulent Taylor vortices. Van Gils *et al* [19] visualized the flow structures in a turbulent TC flow with low-concentration small bubbles (the gas volume concentration is less than 0.1%). The left panel of figure 4 shows a snapshot of the high-speed recording of the distribution of the bubbles (the bubble diameter is less than 1 mm). As observed in the figure, these small bubbles clearly do not distribute uniformly in the flow. Most of the bubbles aggregate in the centre of the vortices, even at this very high Reynolds number ($Re_i = 1.2 \times 10^6$). Using image analysis techniques, van Gils *et al* [19] measured the dominant axial wavelength as explained in the figure caption.

Special attention must be paid to this technique. Many studies have suggested that the injection of bubbles can induce drag reduction in TC flows. One mechanism of the drag reduction is that the rising bubbles destroy the coherent structures and induce drag reduction [24]. In order to avoid the modification of flow structures in TC flow due to the small bubble injection, one has to carefully control the experimental conditions for flow visualizations: the rising velocity of the bubbles must be significantly smaller than the flow velocity fluctuations themselves. The volume fraction of the bubbles must be very small to have negligible effects on the flow field. In the experiments of van Gils *et al* [19], the typical rms velocity of the liquid flow is ∼6 m s⁻¹, which is much larger than the rising velocity of the mm-sized bubbles (about 0.3 m s⁻¹), and the volume fraction of the bubbles is much smaller than 0.1%. The global torque (drag) measurement also confirmed that the change of the drag due to the bubble injection in this case is not detectable.
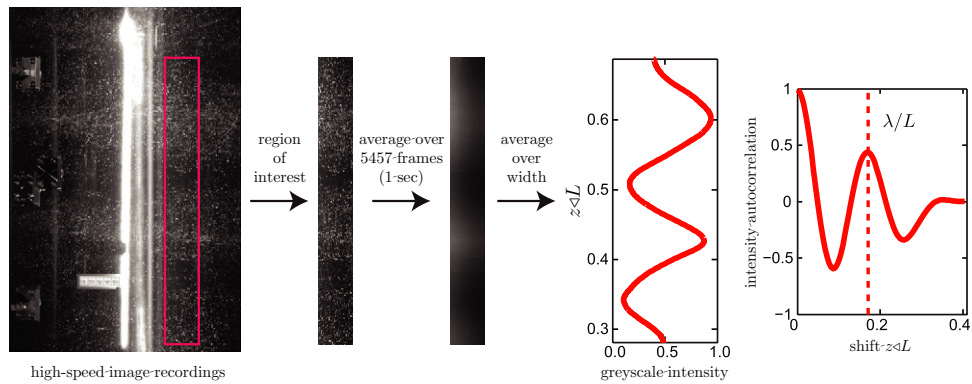
Figure 4. Figures reproduced from [19]. Flow visualization with bubbles with a diameter of 1 mm. Processing steps involved in the high-speed image analysis for measuring the wavelength of the convective rolls ($Re_i = 1.2 \times 10^6$ and $Re_o = 0$). A small amount of bubbles are injected into the flow to act as tracers for vortical structures. The images are recorded at fixed Re_i for 1 s with a high-speed camera operating at 5400 frames per second. A region of interest is selected with a uniformly lit background and the greyscale intensity of this region is averaged over all the frames. Subsequently, by averaging the greyscale intensity over the width, one can get intensity versus the non-dimensional axial position z/L, where L is the height of the TC apparatus. Autocorrelation on this data provides the dominant axial wavelength.

With increasing Reynolds number of the system, the TC system enters highly turbulent regimes. It becomes more difficult to visualize the flow structures with the Kalliroscope flakes or small bubbles. One reason is that the time scale of the velocity fluctuations is very short, and so the flakes/bubbles cannot respond to the rapid variation of the velocity fluctuations. Secondly, the flow structures might be unstable in time, and the transitions between different flow states would be too fast for visualization using the Kalliroscope flakes or small bubbles.

Although flow visualizations provide a global picture of the flow structures in TC flow, quantitative velocity measurements are crucial for studying turbulent TC flow. Many techniques are available to measure the flow velocity inside the TC gap. Below, we review a few intrusive and non-intrusive techniques.

2.2. Intrusive techniques for flow velocity measurements

2.2.1. Pitot tubes. A Pitot tube is a pressure-based measurement instrument, which is widely used to measure air/gas velocities in industrial applications and the airspeed of an aircraft. It is chiefly used to measure the local velocity at a given point in the flow stream as shown in figure 5. The measurement principle is based on Bernoulli's equation: p_t (stagnation pressure) = p_s (static pressure) + p_v (dynamic pressure). The velocity is determined by the difference between the stagnation pressure and the dynamic pressure, i.e. $P_t = P_s + \frac{1}{2}\rho V^2$, or $V = \sqrt{2 \times (p_t - p_s)/\rho}$. The key requirements for the application of this method are: the Reynolds number is sufficiently large that the viscosity does not play a role; and the probe is small enough to satisfy the conditions of strict applicability of the Bernoulli equation. One has to carefully control the experimental conditions to obtain reliable results. For more details about the Pitot tube technique, we refer to [25].

In 1933, Wendt [29] performed velocity profile measurements in a TC apparatus using a Pitot tube at various Re numbers (Re_i and Re_o) up to 10^5, and found that technique was

Figure 5. A schematic illustrating the measurement principle of a Pitot tube. The diameter of the tube is typically of order mm.
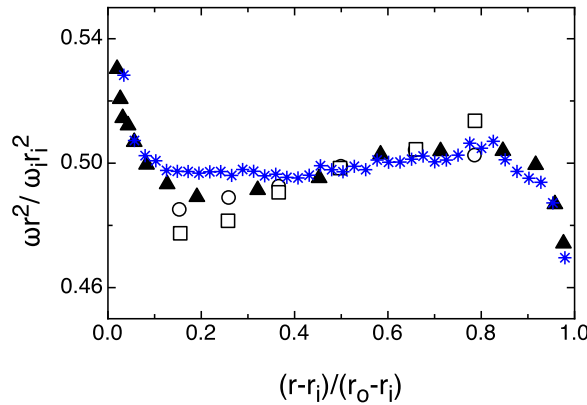

Figure 6. Angular momentum normalized by angular momentum of the IC versus radius for a variety of Reynolds numbers. Measurements with a Pitot tube [26]: squares—$Re_i = 1.8 \times 10^4$, circles—$Re_i = 5.4 \times 10^5$, the radius ratio of the apparatus $\eta = 0.724$. Triangles from Smith and Townsend [27] measured with a hot-film probe at $Re_i = 5 \times 10^4$, and $\eta = 0.666$. Blue stars are the data from van Gils *et al* [28] measured with laser Doppler anemometry (LDA) at $Re_i = 1.0 \times 10^6$.

reliable and robust. Lewis [26] and Lewis and Swinney [30] carried out the angular velocity momentum profile measurements in the bulk region of the TC gap using the Pitot tube (United Sensor PCC-12-KL) technique at IC Re_i up to 5.4×10^5 at the pure IC rotation case. The pressure difference was measured with a simple U-tube and ruler. An uncertainty of 3% in their velocity measurements at low fluid speeds resulted from the accuracy of measuring small height differentials in the U-tube. At higher rotation rates an uncertainty of 1% was determined by the limits of the technique [26]. Figure 6 shows the measured angular momentum profiles as a function of the normalized radial position, the open symbols are the measured data using the Pitot tube. They managed to measure the small amplitude of the angular velocity gradient in the bulk region of the turbulent TC flow. The measurements were only performed in the bulk region, due to the limitations in the probe size and measurement technique [26, 30].

2.2.2. Thermal anemometry. The thermal anemometry technique is widely used to measure rapidly varying velocity fluctuations with a good spatial and temporal resolution. Two types of sensors frequently used for flow velocity measurements are the hot-wire probe and hot-film probe. Hot-wire probes are generally used in gas flow measurements and hot-film probes are generally used in liquid flows. The sensors are typically made from materials like platinum or nickel, which have high specific resistivity, high temperature coefficient of resistance, small heat capacity and high tensile strength.

The measurement principle is based on the change in heat transfer of a small heated sensor exposed to the fluid motion. The change in the sensor resistance can be used to generate a measurable signal. In this technique, three operating modes are possible [25, 31]: constant-current anemometer (CCA), constant-temperature anemometer (CTA) and
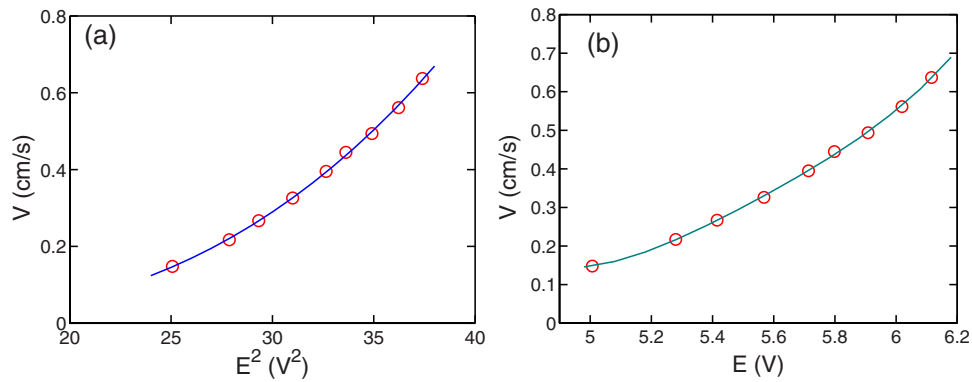
Figure 7. Data from [32]. A typical calibration curve for a cylindrical hot-film probe: (*a*) polynomial curve fitting, and (*b*) power law curve fitting. The velocity values were measured using laser Doppler anemometry (LDA) to be discussed below.
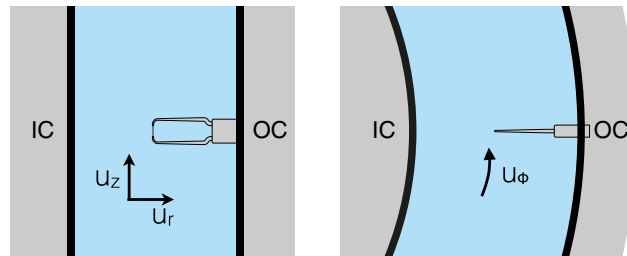

Figure 8. A simplified sketch on a cylindrical hot-film probe inside a TC facility, left: vertical cross-section, right: top view.

constant-voltage anemometer (CVA). Since the constant-temperature mode is frequently used, sometimes hot-film and hot-wire probes are called CTA probes.

The advantages of the thermal anemometry technique include a good frequency response (400 kHz is feasible), a wide velocity range (from low subsonic to high supersonic flow), a high signal to noise ratio, continuous signals, and the possibility of simultaneous temperature measurements [31].

A CTA probe does not directly provide the flow velocity (V). The acquired signal is usually a voltage signal (E), and one has to calibrate the probe to convert the voltage signal into a velocity signal. The two functionals used for the calibration are the polynomial curve fitting $V = C_0 + C_1 E + C_2 E^2 + C_3 E^3 + C_1 E^4$ and power law curve fitting $E^2 = A + B V^n$ (King's law), where C_0, C_1, C_2, C_3, C_4, A, B and n are the corresponding fitting parameters. Figure 7 presents an example of the calibration curves using polynomial and power law fits in a turbulent water flow at low velocities.

The thermal anemometry technique has been employed for velocity measurements in turbulent TC flows [26, 27, 30, 33]. The most commonly used probe type was the hot-film probe, and both cylindrical and conical probe geometries have been used for the measurements. Typically cylindrical probes have a dimension of ∼1 mm in length and 100 μm in diameter, and conical ones have a diameter of ∼1.5 mm. Cylindrical probes are more sensitive and conical ones are more rigid. Figure 8 shows a sketch of a cylindrical hot-film probe mounted in a TC apparatus.

Let us assume the flow to be in the following condition: the mean flow is in the azimuthal direction $\langle u_\phi \rangle_t$, and the time-averaged radial and axial velocities are negligible $\langle u_r \rangle_t = \langle u_z \rangle_t = 0$. The hot-film anemometer can only measure the magnitude of the velocity, not the individual components. In the configuration shown in figure 8, the measured velocity amplitude is

$$u_{\text{eff}} = \sqrt{u_\phi^2 + u_r^2}, \tag{11}$$

where the u_ϕ and u_r are azimuthal and radial velocity components respectively. In turbulent TC flow with only IC rotation, the flow satisfies the following conditions: $\langle u_\phi \rangle_t$ is the dominant component, and the velocity fluctuations are much smaller than the mean flow velocity, i.e.

$$\langle u_\phi \rangle_t \gg \langle u_r \rangle_t, \tag{12}$$

$$\langle u_\phi \rangle_t \gg \sqrt{\langle u_\phi'^2 \rangle_t}, \tag{13}$$

where $u_\phi' = u_\phi - \langle u_\phi \rangle_t$. In this case, the azimuthal velocity can be measured using a hot-film anemometer with a good accuracy $u_{\text{eff}} \simeq u_\phi$. Figure 6 shows a comparison of angular velocity profiles in turbulent TC flow at only IC rotation measured with a hot-film probe [27] and a Pitot tube [26]. A good agreement between the two methods is found in the bulk regime, and the measured results are in reasonable agreement with the results measured using laser Doppler anemometry—LDA (to be discussed below) [28]. The hot-film probe also allows the measurement positions to be closer to the inner and outer walls compared to the Pitot tube.

The situation becomes complicated when the OC is also in rotation. The azimuthal velocity could be very small for a counter-rotation turbulent TC flow, i.e. $\langle u_\phi \rangle_t \simeq 0$. The measured velocity fluctuations can no longer be assumed to be mainly contributed by the azimuthal component. We have already noted that the hot-film anemometer does not provide information on the direction of the velocity. The velocity fluctuations around a zero mean flow cannot be well quantified with the hot-film anemometry. In bubbly flow system, a flying hot-film anemometry technique is used to overcome this issue. The sensor used is mounted on a sled, which is translated into the flow at a constant linear velocity [34]. However, it is not straightforward to implement this idea in the TC geometry. For TC with gases as working fluids, one can implement multiple hot-wire probes to measure the velocity components and the velocity gradient [35].

2.3. Non-intrusive techniques for flow velocity measurements

The Pitot tube and hot-film probe techniques can be used to measure the flow velocity inside the TC gap, but they suffer from drawbacks. These techniques measure the magnitude of the velocity, not the individual components, and lack directional information when a single probe is used. In addition, the flow is altered since they are intrusive measurement techniques. This is not a serious issue for non-recirculating setups, like an open-ended water/wind tunnel, but it can be a severe consequence in closed systems, such as a rotating drum [36], RB convection [14], and in a TC apparatus. It is well known that these probes can induce vortices, either in the form of a von-Kármán vortex street or as a turbulent wake depending on the Reynolds number and the detailed geometry. In a rotating drum experiment, Sun *et al* [36] found that these vortices can survive a full revolution of the system. Of course, there are also some non-intrusive probe-based techniques for flow measurements, like flush-mounted shear stress probes on a surface [26, 30].

LDA [37], particle tracking velocimetry (PTV) [38, 39] and particle imaging velocimetry (PIV) [40, 41] are optical techniques, which are discussed below in detail. These methods, by

their very nature, are non-intrusive and do not disturb the measured flow under consideration. In addition, these techniques can measure the individual velocity components and have directional sensitivity.

The addition of seeding particles is imperative for these techniques, and one should check whether these particles can accurately follow the flow. In order to ensure this, the particle Stokes number, defined as the ratio between the characteristic response time of the particle and the characteristic flow time scale [21], should be small enough. From a practical point of view, the measurement errors for velocity are below 1% when the particle Stokes number is less than 0.1 [25]. The key question in a TC flow is whether the centrifugal force on the seeding particles has a major effect on the particle movements. In [28], the seeding particles (PSP-50 Dantec Dynamics) have a mean radius of $r_{seed} = 2.5\,\mu$m and a density of $\rho_{seed} = 1.03\,$g cm^{-3}. We estimate the maximum velocity difference $\Delta v = v_{seed} - v_{fluid}$ between a tracer particle v_{seed} and its surrounding fluid velocity v_{fluid}. This velocity difference is assumed for the drag force $F_{drag} = 6\pi\mu r_{seed}\Delta v$ to outweigh the centrifugal force $F_{cent}(r) = 4\pi r_{seed}^3(\rho_{seed} - \rho_{fluid})v^2/(3r)$. We put in $v = 5\,$m s^{-1} as a typical azimuthal velocity in the TC-gap at the mid-gap radial position $r = 0.24\,$m, with $\rho_{fluid} = 1000\,$kg m^{-3} as the fluid density and $\mu = 9.8 \times 10^{-4}\,$kg ms^{-1} as the dynamic viscosity (water at 21 °C). This results in a velocity difference $\Delta v = 2r_{seed}^2(\rho_{seed} - \rho_{fluid})v^2/(9\mu r) \approx 5 \times 10^{-6}\,$m s^{-1}, which is several orders of magnitude smaller than the typical flow velocity fluctuation of order $10^{-1}\,$m s^{-1} and therefore the centrifugal force acting on the seeding particles used in van Gils *et al* [28] is negligible. In individual experiments, one has to carefully check the properties of the tracer particles and the flow properties to ensure that the particle velocity faithfully reflects the true velocity of the flow.

2.3.1. Laser Doppler anemometry.   LDA, as its name suggests, is based on the Doppler effect, which is familiar to all of us having heard the sirens of an emergency vehicle passing by. The same phenomenon occurs with light, though the change in colour is generally not observable by eye. The difference between the original frequency and the scattered frequency is called the Doppler shift f_d. This shift depends on the velocity of the particle, the wavelength of the light, and the position of the observer with respect to the source. A way of measuring the velocity would be to measure this Doppler shift directly, this is in practice however very difficult because the frequency shift is only a tiny fraction of the original frequency. The most commonly used version of LDA is a so-called dual beam heterodyne configuration, which solves this problem. In this configuration two beams are focused in one position: the measurement volume. A particle passing through the measurement volume will scatter light from both beams. The frequency shift is different for each beam, because the velocity vector makes a different angle for each beam and the observer. We call the Doppler frequency of beam 1 as f_{d_1}, and for beam 2 as f_{d_2}. Because both f_{d_1} and f_{d_2} are small as compared to f, the scattered signals have a similar frequency. The Doppler frequency can now be found by measuring the frequency difference between two beams, which can be done with high accuracy with a photo detector. The Doppler frequency is given by [42, 43]:

$$f_d = \frac{2\sin(\theta/2)}{\lambda}|v_k|, \tag{14}$$

where θ is the angle between the two laser beams, and v_k is the component of the velocity that is along $k_1 - k_2$, where k_i are the propagation vectors of the laser beams.

In order to add directional information one shifts the frequency of one original beam, and this is accomplished using a Bragg cell. More details about the LDA in general, the Bragg cell, and the fringe-model, can be found in, e.g., [42–44].
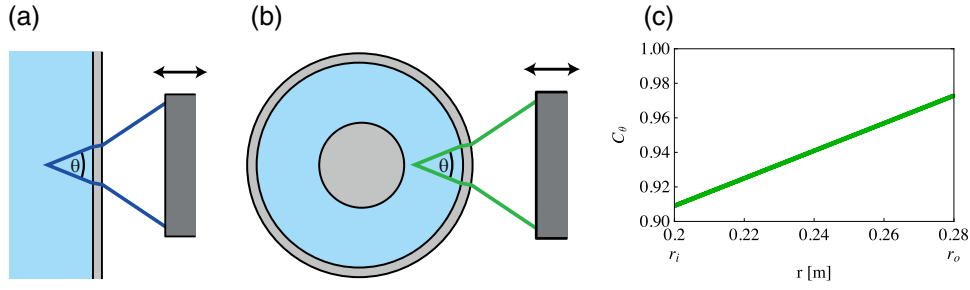
Figure 9. Figure reproduced with permission from [45]. © 2012 Elsevier Masson SAS. All rights reserved. (*a*) Typical beams of the LDA system (equivalent to the vertical plane in the current application): the beams are passing through flat interfaces, and θ does not vary with laser-head position. (*b*) Laser beams are affected by the curved interfaces (horizontal plane for TC flow), and therefore θ is a function of radial position. (*c*) Correction factor C_θ (see equation (16)) as a function of the radial position r calculated with the T^{3}C geometrical parameters. In this case, the azimuthal velocity u_ϕ has to be corrected: $u_{\phi,\mathrm{real}} = C_\theta(r) u_{\phi,\mathrm{measured}}$.

In most situations, the LDA laser beams travel through flat surfaces, as shown in figure 9(*a*). In this case, by invoking Snell's law equation (14) can be simplified as:

$$\frac{f_d}{2|v_k|} = \frac{\sin(\theta_w/2)}{\lambda_w} = \frac{\sin(\theta_a/2)}{\lambda_a}, \tag{15}$$

where the subscripts with 'w' denote quantities in water, and 'a' in air. Equation (15) only holds when the interfaces are flat; it is only then that $\theta_a/2$ is the incidence angle and $\theta_w/2$ the angle of refraction. The changing of the wavelength absorbs the difference in refractive index, i.e. $\sin(\theta_w/2)/\sin(\theta_a/2) = \lambda_w/\lambda_a$. So in the case of flat interfaces, θ_a can be directly calculated from the beam separation and the focal length, and the light frequency/wavelength λ_a. The velocity can be quantified from the Doppler shift (equation (15)). The refractive indices of the container and the working fluid are not used in the calculation of the velocity.

When the interface surface is curved (see figure 9(*b*)), equation (15) is no longer valid anymore to transform θ_w to θ_a. Therefore, the measured velocity needs to be corrected by multiplication with a correction factor, i.e. $u_{\mathrm{real}} = C_\theta u_{\mathrm{measured}}$, and C_θ is

$$C_\theta = \frac{n_a \sin(\theta_a/2)}{n_w \sin(\theta_w/2)}. \tag{16}$$

To determine the correction factor, one can theoretically derive the trajectory of the laser light, see e.g. [46]. However, this analysis becomes very complicated if the system has more than one interface (e.g. multiple OCs). Huisman *et al* [45] built a ray-tracer to correct for two parameters: the angle θ_w for the beam pair in the horizontal plane, and the position of the foci of the beam pair in the horizontal plane, respectively. Using the geometrical parameters of T^{3}C apparatus, Huisman *et al* [45] calculated the correction factor C_θ (see equation (16)) as a function of the radial position r, as shown in figure 9(*c*). Note that the focal position also changes due to the curved surface, and see Huisman *et al* [45] for further details.

The results obtained from the ray-tracer were verified by measuring a well-known solid body rotation state in TC flow, when the IC and OCs are both rotating at the same angular velocity ω. The fluid has a velocity $u_\phi = \omega r$, and $u_z = u_r = 0$ after a sufficient developing time. As an example, the results of the azimuthal velocity versus radial position for $\omega/(2\pi) = 2\,\mathrm{Hz}$ measured by Huisman *et al* are shown in figure 10. The measured velocity profile without corrections is shown in red squares, which is higher than the actual solid-body
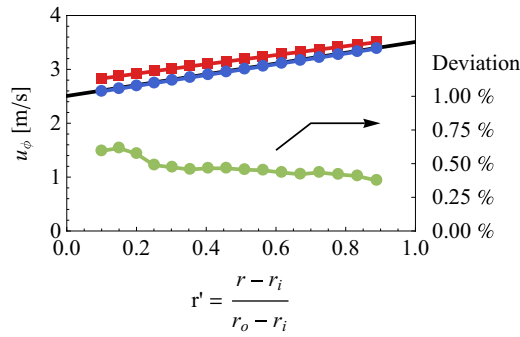
Figure 10. Figure reproduced with permission from [45]. © 2012 Elsevier Masson SAS. All rights reserved. In red squares the *uncorrected* azimuthal velocity as a function of radial position is shown, and in blue dots the *corrected* azimuthal velocity. The black solid line is the theoretical flow profile $u_\phi = \omega r$, the deviation from this profile is plotted with green dots, the corresponding scale is on the right. The theoretical and corrected measured profiles are found to be in good accordance.
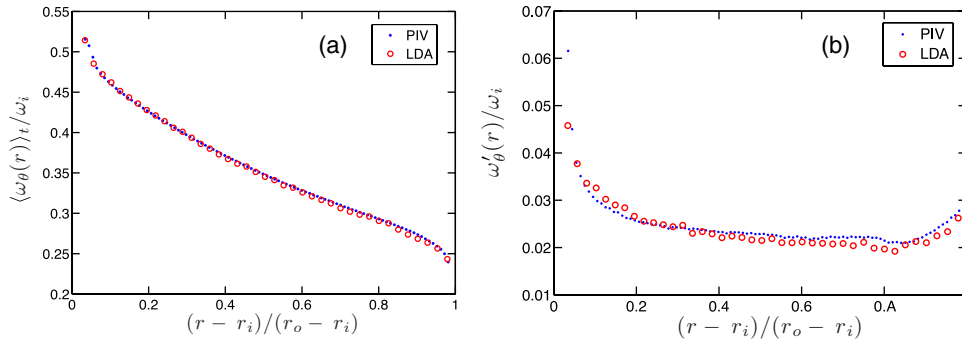

Figure 11. Data from [28]. Radial profiles of the azimuthal angular velocity measured at the middle height $z/L = 0.5$, plotted against the dimensionless gap distance $\tilde{r} = (r - r_i)/(r_o - r_i)$ for $Re_o = 0$ and $Re_i = 1 \times 10^6$. (*a*) The time-averaged angular velocity $\langle \omega(\tilde{r}) \rangle_t$ normalized by the angular velocity of the inner wall ω_i. (*b*) Standard deviation of the angular velocity $\sigma_\omega(\tilde{r})$ normalized by the angular velocity of the inner wall. The boundary layers at the cylinder walls are not resolved. The open circles correspond to LDA measurements, and the solid dots are the measured data obtained using the PIV technique (to be discussed below).

profile (the black line). The data points (blue circles) are found to agree well with the actual flow profile within 0.75% after applying the beam angle correction. The remaining small deviation could be due to various reasons, e.g. spatially inhomogeneous refractive index in the working fluid, optical misalignment or imperfection, among others. It is clear that the ray tracer correction is crucial for reliable velocity measurements in TC flow.

Figure 11 shows the radial profiles of the azimuthal angular velocity and its standard deviation at a very high Reynolds number ($Re_i = 1 \times 10^6$) measured using LDA. The flow inside the gap is in a highly turbulent state, and the LDA has proven to be an excellent tool for the measurements of turbulent velocity and its fluctuations in TC flow [28].

2.3.2. Particle image velocimetry. It has been shown that the PIV technique is a powerful tool for direct measurements of the flow field in turbulent flows. The flow is seeded with tracer
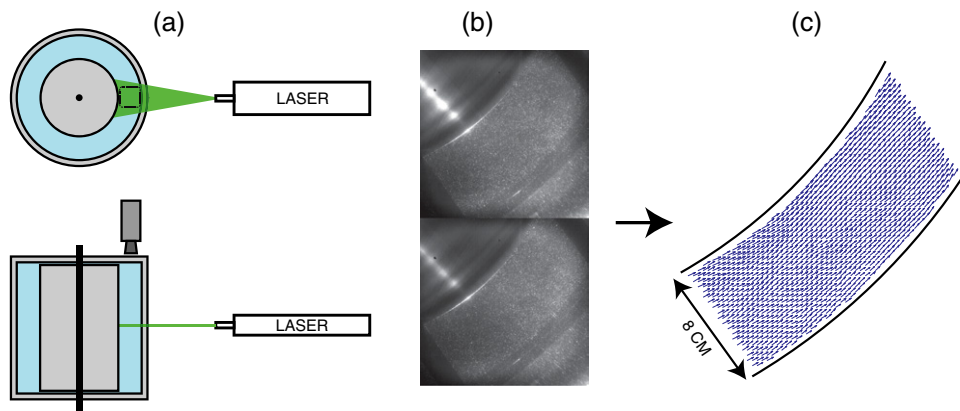
Figure 12. Figure reproduced from [49]. (*a*) 2D-PIV implementation in the T^{3}C. Upper panel: horizontal cross-cut of the setup. The setup is illuminated from the side, which is possible due to the transparent OC. The camera is mounted on top. Lower panel: vertical cross-cut of the setup. The laser beam is reshaped into a sheet with a cylindrical lens, which illuminates part of the area between the two cylinders at a specific height. (*b*) High speed recordings of two consecutive frames. These images are the input for the PIV-analysis. (*c*) The resulting vector field after the PIV-analysis. The difference between two corresponding particles (lightened pixels) on the left is converted into a displacement vector on the right.

particles, whose movements are used to indicate the fluid velocity. The mean displacement of the particles in a small interrogation window is quantified by the cross correlation of two consecutive images with a known time interval. The particles must satisfy the various criteria for the specific experiment conditions, as discussed previously.

The advantages of the PIV technique are: robustness, high accuracy, and the ability to do an entire field measurement. The robust nature of PIV stems from its conceptual simplicity. It directly measures two variables: displacement and time increment, which are the fundamental variables for the definition of velocity [47]. In contrast, a hot-film anemometer measures rate of heat transfer from the heated element in the fluid, and LDA measures the Doppler shift of scattered light from tracer particles. For the details on PIV, we refer to [47, 48].

PIV is a powerful tool for the study of flow structures and velocity profiles in turbulent TC flow. However, it is not straightforward to implement PIV in TC. Here we describe two examples where the PIV has been employed in turbulent TC flows.

Huisman *et al* [49] measured the azimuthal and axial velocity components in highly turbulent TC flow of Re_i up to 10^6. The experiments were performed in the T^{3}C facility [20] with gap width of 7.9 cm. They utilized the viewing ports in the top plate of the apparatus to measure the flow from above. The experimental setup is shown in figure 12(*a*) with the side and top views. The flow was illuminated from the side using a pulsed laser (Litron LDY 300 Series, dual-cavity, pulsed Nd : YLF PIV Laser System), creating a horizontal laser sheet. The working fluid (water) was seeded with 20 μm polyamide seeding particles, and was recorded using a high-speed camera (FastCam 1024 PCI), operating at 1024 pixel × 1024 pixel resolution at frame rate of $f = 1$ kHz. To have a Δt (the time interval between two consecutive images) far smaller than $1/f$ (f is the frame rate), the PIV system was operated in the double-frame mode, i.e. two particle images are recorded on two frames.

Figure 12(*b*) shows two image pairs, and the velocity map corresponding to these two images computed from the Lavision PIV software (DAVIS 7.3) is shown in figure 12(*c*).
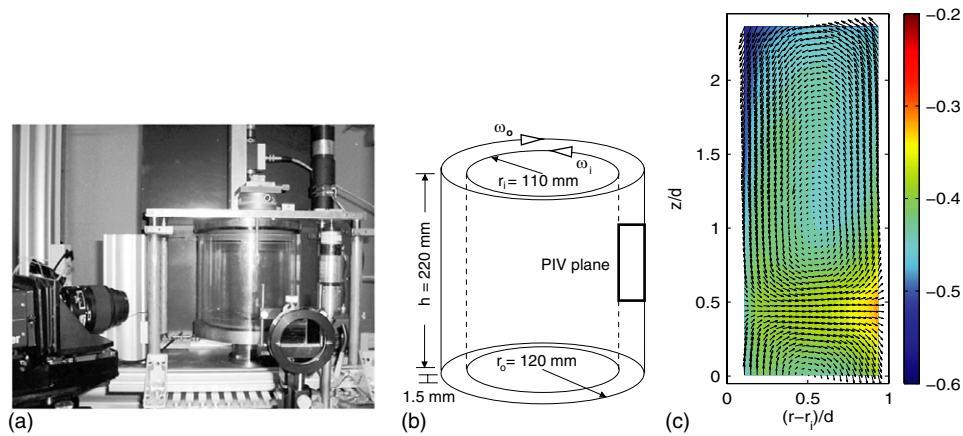
Figure 13. Reproduced with permission from [41]. Copyright 2010, AIP Publishing LLC. (*a*) Photograph and (*b*) sketch of the TC setup, along with dimensions of the experimental setup. One can see one of the two cameras (left side), and the light sheet arrangement (right side). The second camera is further to the right. (*c*) An example of the time-averaged flow at $Re = 1.4 \times 10^4$ with only IC rotation. Arrows indicate radial and axial velocities; colour indicates azimuthal velocity normalized with inner wall velocity.

The PIV measurements provided direct access to both the angular velocity $\omega(\phi, r, z, t) = u_\phi(\phi, r, z, t)/r$ and the radial velocity $u_r(\phi, r, z, t)$ simultaneously. The solid dots in figure 11 show the profiles of the angular velocity and its standard derivation from the PIV measurements. Excellent agreement is found from the LDA and PIV measurements. In addition, PIV measurements can provide the statistics of the radial velocity component, which will be discussed below. When measuring from the top view, one has to pay careful attention to the out-of-plane velocity components, which in this context is in the axial (vertical) direction. The ratio of the vertical velocity and the azimuthal velocity varies significantly for different rotation ratios $a = -\omega_o/\omega_i$. For the pure inner rotation case, the azimuthal velocity component is 1–2 orders of magnitude larger than the vertical one, therefore the out-of-plane motion is not important. But in the counter-rotation situations, the vertical velocity could be as large as the azimuthal one. Here, one has to pay special attention to the choice of Δt (the time interval between two consecutive images) by checking the quality of the cross-correlation map in the individual cases.

The top view PIV measurements cannot provide the flow field in the radial and axial (r, z) plane simultaneously. One has to view from the side to measure the flow structures in the (r, z) plane. In RB flow, one can mount a square 'jacket' outside of the RB system to reduce the distortion due to the curved surface [50]. In TC flow, since the OC is usually in rotation, it is not desirable to place the system in a box. However, the image distortion due to the curved surface can be corrected by calibrations [41].

Ravelet *et al* [41] measured three components of the velocity using stereoscopic PIV in a vertical plane of TC flow at a Reynolds number of $Re = 1.4 \times 10^4$. The experimental setup is indicated in figures 13(*a*) and (*b*). The measurement plane was vertical, i.e. normal to the mean flow: the in-plane components are the radial (u_r) and axial (u_z) velocities, while the out-of-plane component is the azimuthal component (u_ϕ). The measurement plane was illuminated using a double-pulsed Nd : YAG laser with a light-sheet thickness of 0.5 mm. The tracer particles they used were 20 μm fluorescent spheres. The measurement plane was imaged from both sides with an angle of 60° (in air) using two double-frame CCD (charge coupled device) cameras on

Scheimpflug mounts. The field of view in their experiments was $11 \times 25\,mm^2$ as indicated in figure 13(*b*). They took special care regarding the calibration procedure, because the evaluation of the plane-normal azimuthal component heavily depends on the calibration [41]. They used a thin polyester sheet with printed crosses as a calibration target, and attached this target on a rotating and translating stage. The calibration target was first put into the light sheet and traversed perpendicularly to it. Typically, they took five calibration images with intervals of 0.5 mm. The raw PIV images were processed using DAVIS 7.2 (Lavision Inc.) using a multigrid algorithm, with a final interrogation area of 32×32 pixels and 50% overlap. Then, the three velocity components were reconstructed based on the two camera views. Figure 13(*c*) shows an example of the time averaged flow at $Re = 1.4 \times 10^4$ with only IC rotation. The strong secondary mean flow in the form of counter-rotating vortices is clearly visible in their measurements.

Overall, the PIV technique is an excellent tool for the measurement of the velocity profile, flow velocity structures, and statistics of velocity fluctuations in turbulent TC flow. One can also measure the local transport fluxes using PIV, which we will discuss below.

2.4. Global torque and local angular velocity flux

2.4.1. Global torque measurements. The global torque on the cylinders in a TC setup can be measured by monitoring the power of the driving motors [51]. However, the technique suffers from several drawbacks, since it does not account for the drag from the bearings and seals, the efficiency losses, and the drag from the end sections [52]. A better approach for the global torque measurements is to use a strain gauge load-cell. A strain gauge is a long length of resistor arranged in a zigzag pattern on a membrane. When the strain gauge is stretched, its resistance increases. The strain gauges are mounted in a frame and often in four pieces to form a full 'Wheatstone Bridge', as shown in figure 14(*a*). In this configuration, a downward bend stretches the gauges on the top and compresses those on the bottom. The variations of the resistances of the strain gauges are transferred into a voltage signal (sketched in figure 14(*b*)) and amplified to yield the output signal.

Here we use the T^3C apparatus as an example of the torque sensor mounting and calibration. A metal arm, consisting of two separate parts, is rigidly clamped onto the drive axle and runs to the inner wall of the IC section. The split in the arm is bridged by a parallelogram load cell (see figure 14(*c*)). Calibration of the load cells is done by repeated measurements, in which a known series of monotonically increasing or decreasing torques is applied to the IC surface, as shown in figure 15(*a*). The IC is not taken out of the frame and is calibrated *in situ*. The torque is applied by strapping a belt around the IC and hanging known masses on the loose end of the belt, after having been redirected by a low-friction pulley to follow the direction of gravity. Figure 15(*b*) shows the calibration data for one load cell (LSM300, Futek Inc.) in the T^3C system. The three independent calibration data nicely collapse. The line in the figure is the best fit of the data using third-order polynomial fitting. The errors between the measured data and the fitting curve are shown in figure 15(*c*). The majority of the fitting errors are less than 0.2 Nm. However, one should pay attention to the hysteresis of the load cell. These three data sets were measured with monotonically increasing the load. The data were found to be different with decreasing the applied torque, suggesting that the hysteresis is not negligible for the torque calibrations and measurements. The maximum deviation due to hysteresis is found to be around 2 Nm, which is 10 times larger than the fitting errors for monotonically increasing torque. To avoid hysteresis, it is desirable to perform experiments with monotonically increasing or decreasing torque. Otherwise, one should calibrate the load cell for both increasing and decreasing torque respectively.
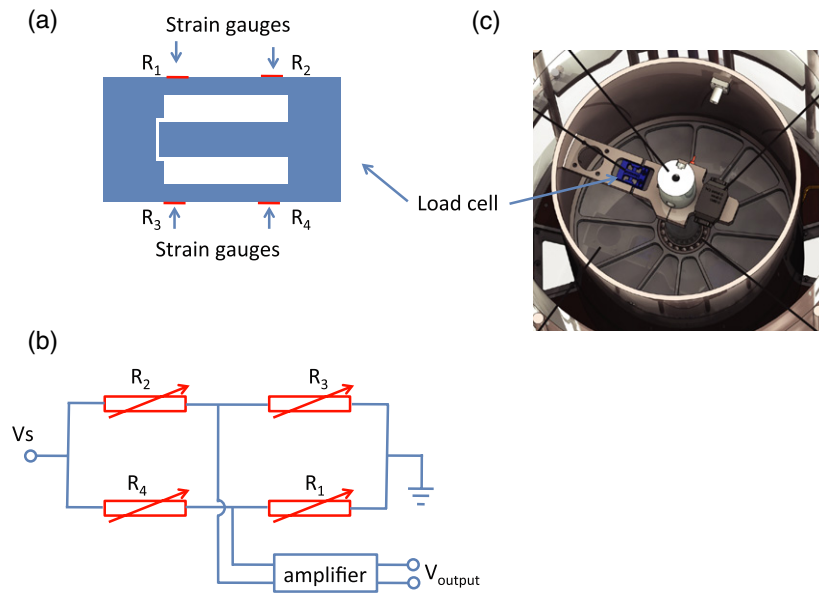
Figure 14. (*a*) A sketch of a load cell and the strain gauges. (*b*) A sketch of the electrical circuit of the load cell. (*c*) Reproduced with permission from [20]. Copyright 2011 AIP Publishing LLC. Horizontal cut-away showing the load-cell construction inside the IC_{mid} drum. The load cell spans the gap in the arm, connecting the IC drive axle to the IC wall.
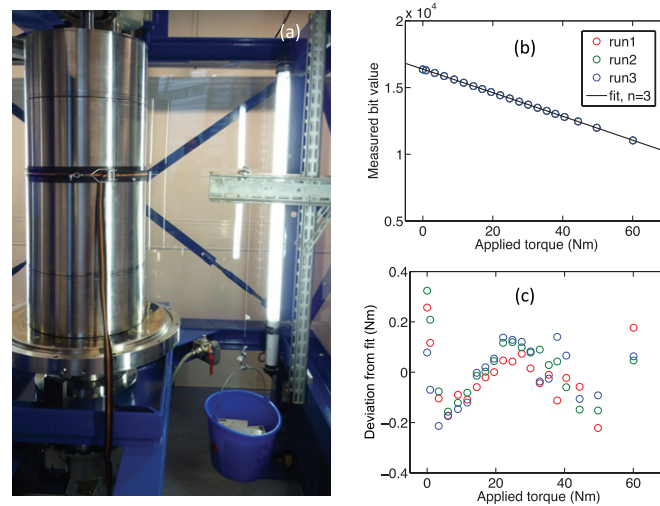

Figure 15. Figure reproduced from [53]. (*a*) A photograph of the T^3C showing that the load cells are calibrated in situ. (*b*) The calibration data for one load cell (LSM300, Futek Inc.) mounted in the T^3C facility. The data were measured by monotonically increasing the applied load. (*c*) The corresponding fitting errors of the calibration.

Figure 16 shows one example of Nu_ω versus Ta for various a measured in the T^3C facility by van Gils *et al* [54]. A *universal* effective scaling $Nu_\omega \propto Ta^\gamma$ with $\gamma \approx 0.38$ is clearly revealed. And this efficient exponent does not depend on the control parameter 'a'. This corresponds to a scaling of $G \propto Re_i^{1.78}$ for the dimensionless torque [52], to $c_f \propto Re_i^{-0.24}$
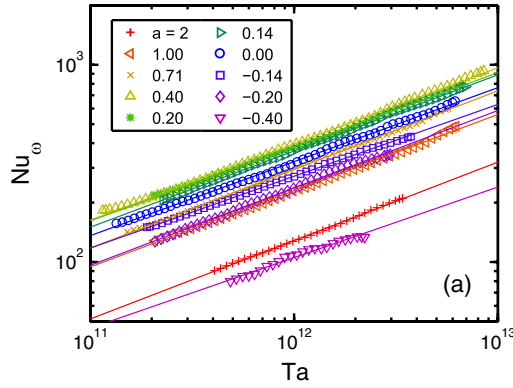
Figure 16. Figure reprinted with permission from [54]. Copyright 2011 by the American Physical Society. Nu_ω versus Ta for various a: a universal effective scaling $Nu_\omega \propto Ta^{0.38}$ is revealed.

for the drag coefficient, and to $G \propto Ta^{0.88}$ [54]. We refer readers to [28, 54–56] for further details about the global torque versus the control parameters.

2.4.2. Local angular velocity flux measurements based on velocity correlation. One also can indirectly obtain the torque value by measuring the correlation of the radial and angular velocity fluctuations. The condition is that the angular velocity (or azimuthal velocity) and radial velocity must be measured simultaneously at the same physical point, which can be realized using LDA [57, 58] or PIV [59].

In turbulent TC flow, the (total) angular velocity flux (convective + diffusion) is

$$J^\omega(\phi, r, z, t) := r^3 \left(u_r \omega - \nu \partial_r \omega \right). \tag{17}$$

In the turbulent regime the convective term is the major contributor to the flux in the bulk [28]. The measurements of the angular velocity flux $J^\omega(\phi, r, z, t)$ in turbulent TC flow at the bulk regime can be simplified as

$$J^\omega(\phi, r, z, t) \sim r^3 u_r \omega, \tag{18}$$

which is made dimensionless by its value for the laminar non-vortical flow, $J_{\text{lam}}^\omega = 2\nu r_i^2 r_o^2 (\omega_i - \omega_o)/(r_o^2 - r_i^2)$, giving the local 'Nusselt number' (see [2])

$$Nu_\omega(\phi, r, z, t) = J^\omega(\phi, r, z, t)/J_{\text{lam}}^\omega. \tag{19}$$

This $Nu_\omega(\phi, r, z, t)$ is the local convective angular velocity flux. One must note that an additional *axial* average is required to have the exact relation between Nu_ω and the global torque τ that is required to obtain the IC at constant velocity ([2]),

$$\tau = 2\pi L \rho J_{\text{lam}}^\omega \langle Nu_\omega \rangle_{\phi, z, t}. \tag{20}$$

Huisman *et al* [59] directly measured the local angular velocity flux in the turbulent TC flow using PIV. The measurements were done in the case of IC rotation at mid-height of their TC apparatus $z = H/2$. For three different rotation rates $\omega_i/(2\pi) = 5\,\text{Hz}$, $10\,\text{Hz}$ and $20\,\text{Hz}$ (corresponding to $Ta = 3.8 \times 10^{11}$, 1.5×10^{12} and 6.2×10^{12}) they measured the local velocity from the top of their TC apparatus. One example of the velocity map is shown in figure 12(*c*). The local velocity $\vec{u}$ is then decomposed into the angular velocity $\omega(\phi, r, z, t)$ and the radial velocity $u_r(\phi, r, z, t)$ by aligning the ϕ direction to $\langle \vec{u} \rangle_t$. The corresponding local $Nu_\omega(\phi, r)$ is obtained based on equations (18) and (19). In figure 17
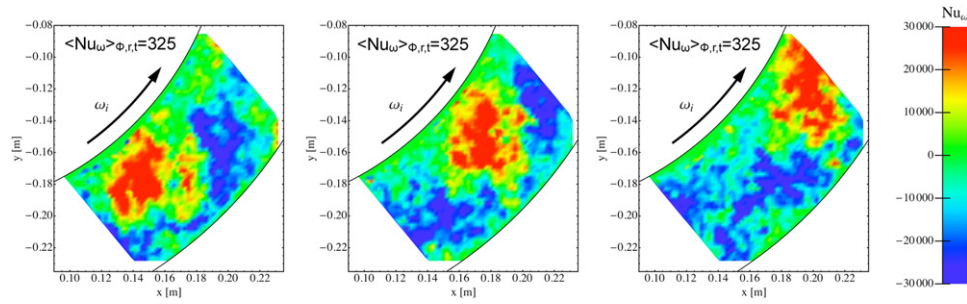
Figure 17. Figure reprinted with permission from [59]. Copyright 2012 by the American Physical Society. Snapshots of the instantaneous convective angular velocity flux, measured at $z = L/2$, for $Ta = 1.5 \times 10^{12}$. The (r, ϕ)-plane and time averaged flux is found to be equal to $\langle Nu_\omega \rangle_{\phi,r,t} = 325$.

we show several snapshots of $Nu_\omega(\phi, r)$ at mid-height $z = L/2$ for $Ta = 1.5 \times 10^{12}$. The quantity of $Nu_\omega(\phi, r)$ shows *huge* fluctuations, ranging from $+10^5$ to -10^5 and even beyond, whereas the time-averaged $\langle Nu_\omega(\phi, r, t) \rangle_{\phi,r,t} = 325$ is found to be very close to the globally measured value $Nu_\omega^{\mathrm{glob}} = 326 \pm 6$ obtained from the load cell [54]. The instantaneous local flux fluctuations can thus be more than ± 300 times as large as the time-averaged flux. Such large fluctuations have also been reported for the local heat-flux in RB flow [60], but in that case the largest fluctuations were only 25 times larger than the mean flux. The fluctuation amplitudes will of course depend on the control parameters of the system.

2.5. Two-phase (bubbly) TC flow

The injection of bubbles offers a new direction in the study of TC flows. There is huge interest in drag reduction, since it can lead to significant reduction of the fuel consumed by ships without adding contaminating substances into water [61]. The TC system is an ideal test bed for studying the drag that a surface experiences when moving in a bubbly flow [62–65]. The experimental challenges in bubbly TC flows are to locally measure and quantify the bubble size and distribution.

Although one can measure the bubble size and distribution with the particle tracking velocimetry technique in the very dilute ($<1\%$) bubbly flow [32,66], the optical fibre technique is mainly used for bubble detection in bubbly flows [67–74]. The optical probe is a local phase detection device, which can distinguish between water and air. The light emitted by a light source is sent through one extreme of the optical fibre. When the light reaches the other extreme of the fibre (treated to have a specific geometry—the so called tip) a part of the light is reflected. The reflection coefficient depends on the refractive index of the phase in which the fibre tip is submerged. By measuring the amount of reflected light over time, one can obtain bubble statistics. For a detailed description of the working principle, we refer to [75].

In their experiments on bubbly TC flow, van Gils *et al* [76] used a custom made glass fibre probe (0.37 NA Hard Polymer Clad Multimode Fibre, Thorlabs Inc., diameter of $200\,\mu$m), whose tip has a smooth U-shaped dome, as shown in figure 18(a). A photodiode was used to measure the internally reflected light from the optical fibre. In the work of van Gils *et al* [76], the configuration of the optical fibre in the T^{3}C system is shown in figure 18(b). The optical probe passed through a small hole of the OC with the fibre tip, and was placed inside the TC gap, and parallel to the azimuthal axis.

Figure 19(a) shows a snapshot of the bubble distribution in the T^{3}C at $Re_i = 5.1 \times 10^5$ with stationary OC. Figure 19(b) shows the typical voltage signal from an optical fibre in a
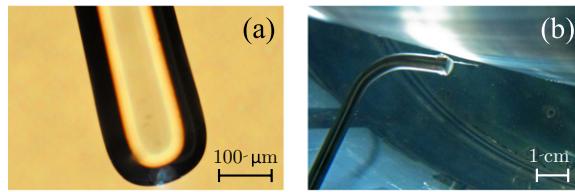
Figure 18. Figure reproduced with permission from [76]. (*a*) Microscope photograph of the fibre tip. (*b*) T^{3}C gap—top view: mounted optical fibre probe to measure the local gas volume fraction close to the IC wall.
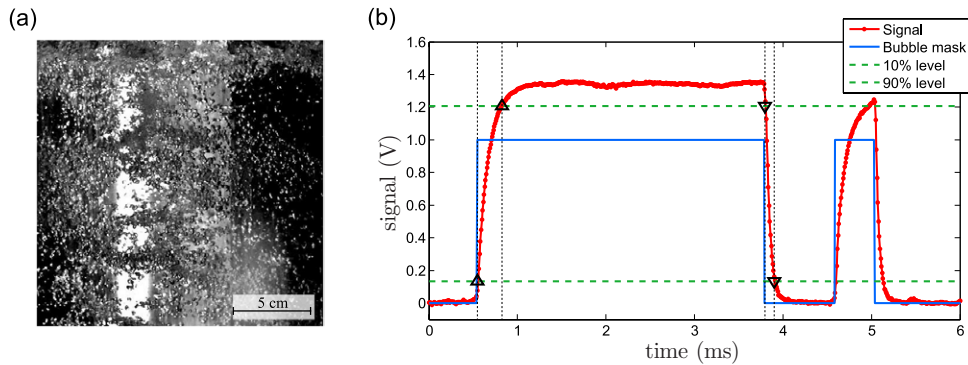

Figure 19. Figure reproduced with permission from [76]. (*a*) A snapshot of the bubble distribution in the T^{3}C, $Re_i = 5.1 \times 10^5$. The OC is stationary. (*b*) Typical measured voltage signals (red lines with dots) of bubble–probe interactions as acquired by the fibre probe placed inside the T^{3}C facility operated at $Re = 5.1 \times 10^5$ and the gas volume concentration of 3%, displaying two distinct bubbles. The signal is acquired at a sampling rate of 120 kHz.

bubbly TC flow. One can clearly see the voltage peaks with different heights and widths. In order to detect the bubbles, one can analyse the peaks with a magnitude above a threshold value. In the present example, the threshold value is selected to be 1 V. The voltage data points above the threshold value are assumed to correspond to the fibre tip immersed in air. The bubble mask built on this threshold value in the present case is shown with the solid blue lines. The width of the bubble mask is then measured by the residence time T_{bubble} per specific bubble, and the bubble size and local gas concentration can be calculated, see [76] for further details. As shown in figure 19(*b*), a positive signal slope of the voltage signal reflects the dewetting process of the fibre tip, and the rewetting process is indicated by the voltage drop (negative slope). van Gils *et al* [76] also examined statistics of the rising and fall time, which measure the bubble-probe interaction time. We refer to [76] for further details.

3. Experiments in turbulent RB flow

3.1. Visualization

In the process through which people understand the world, qualitative knowledge is always before precise measurements and abstract theories. Throughout the history of fluid dynamics research, flow visualization has always been an important tool. It has also been used extensively in the fields of engineering, physics, medical science, meteorology, and oceanography.
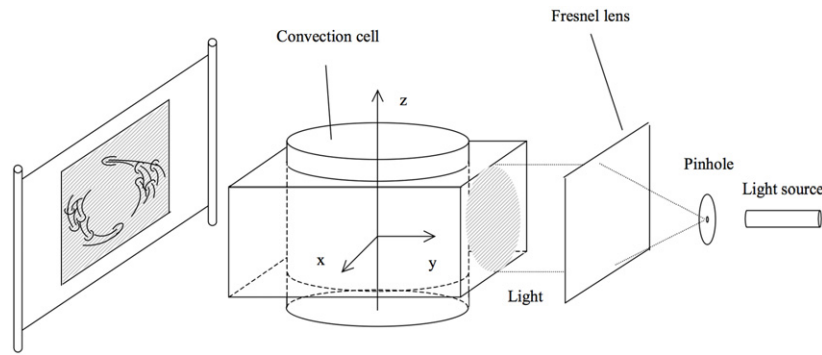
Figure 20. Figure reproduced with permission from [83]. A schematic diagram of the experimental setup for the shadowgraph visualization. When a cylinder is used as the convection cell as shown in the figure, a square-shaped jacket made of flat glass plates is fitted round the sidewall of the cell. The jacket is filled with the same convecting fluid as in the cell. This greatly reduces the distortion effect to the images caused by the curvature of the cylindrical sidewall.

For turbulent RB systems, there are several techniques that have long been used to visualize the global and local flow structures, such as the chemical dying technique [77, 78], the planar-laser-induced-fluorescence (PLIF) technique [79, 80], the shadowgraph technique [81–84], and the thermochromic-liquid-crystal (TLC) technique [85–88]. In this section, we will discuss two visualization techniques: shadowgraph and TLC.

3.1.1. Shadowgraph. The key idea here is that the refractive index of the working fluid depends on temperature and thus parallel light rays either diverge or converge when passing through hot or cold fluids, respectively, and then form dark or bright areas. Figure 20 shows a typical experimental setup used for the shadowgraph visualization. The light source is a white light from a halogen light source. The light first passes through a pinhole in order to produce a point light source. A Fresnel lens then provides a uniform and collimated beam of light to shine through the cell. On the other side of the cell, the image of the flow is seen on a screen made of oil-paper and is captured by a CCD camera placed behind the screen (not shown in the figure). Because the light is not focused onto a specific plane, the projected image on the screen is simply an integration of refractive index contrast along the lightpath. To reduce the effect of light intensity inhomogeneity and other optical imperfections, the shadowgraph is usually divided pixel by pixel by a background image that is taken before the temperature gradient is imposed. The images obtained from the experiments are then rescaled and smoothed.

In the field of turbulent RB convection, shadowgraph is usually adopted to visualize the motion of thermal plumes and the LSC. For example, based on this technique, Xi *et al* [83] revealed that the LSC is a result of the self-organization of the plume motion [83] and Ahlers and co-workers discovered the torsional model of the LSC [91, 92]. Figure 21 shows two examples of shadowgraph visualizations. The left panel is taken from [89]. Thermal plumes are clearly visible from the picture: with hot plumes rising up at the left-hand corner of the bottom plate and cold plumes falling down from the right-hand corner of the top plate. The motion of the plumes at the same time gave us an indication of the existence of the LSC, which moved clockwise along the sidewalls of the cell and dragged the plumes along with it. The right panel of figure 21 is a shadowgraph image showing the spatial structure of the LSC [90]. When viewed from the positive *x* direction the flow is overall a single-roll structure, while the
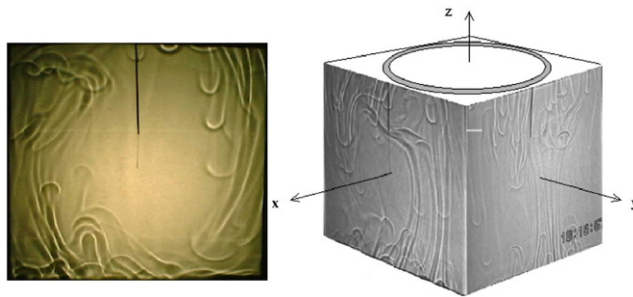
Figure 21. Left panel reprinted with permission from [89]. Copyright 2003 by the American Physical Society. A shadowgraph visualization of the spatial distribution of thermal plumes at $Ra = 6.8 \times 10^8$ and $Pr = 596$ in a $\Gamma = 1$ cylindrical cell. The dark line hanging from the top plate is the thermistor with a stainless steel tube, which was used to measure the temperature at the centre of the cell. Right panel: figure taken from [90]. Shadowgraph images taken simultaneously by two CCD cameras at an angle of $90°$ in a horizontal plane at $Ra = 8.3 \times 10^8$ and $Pr = 1032$ in a $\Gamma = 1$ cell. The convecting fluid is dipropylene glycol in both cases.
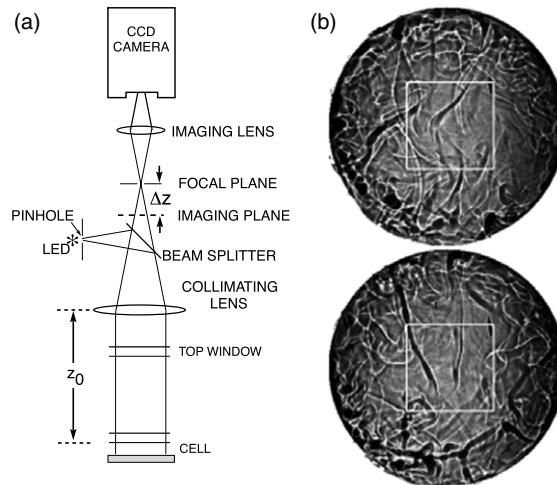

Figure 22. (*a*) Reproduced with permission from [96]. Copyright 1996 AIP Publishing LLC. Schematic diagram of the shadowgraph optics. (*b*) Reprinted with permission from [93] shadowgraph images for $Ra = 5.6 \times 10^8$. Copyright 2004 by the American Physical Society. The elongated black stripes are hot plumes just above the bottom plate. The size of the white box is $31 \times 31 \, \text{mm}^2$.

fluid goes up vertically within a narrow band near the central region of the cell when viewed from the positive *y* direction. The combination of the two views then suggests that the flow in the $\Gamma = 1$ cylindrical cell is a quasi-two-dimensional single-roll structure with a finite width of about half cell diameter.

A similar experimental setup for shadowgraph experiments is shown in figure 22(*a*). Light from a 'point source' is directed into the convection cell by a pellicle beam splitter. The light is then reflected from the cell bottom plate and returns to the optics tower, having passed twice through the fluid layer. It is refocused by the collimating lens and imaged by a lens onto a
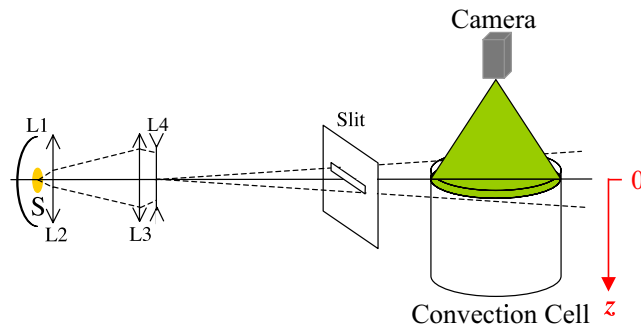
Figure 23. Reproduced with permission from [97]. © IOP Publishing & Deutsche Physikalische Gesellschaft. CC BY-NC-SA. The optical setup for the TLC visualization and measurements: S, halogen lamp; L1, concave mirror; L2 and L3, condensing lenses; L4, diverging cylindrical lens.

CCD video camera. With this technique, Ahlers and co-workers studied the torsional mode of the LSC [93], plume-bulk interactions [94], and two-phase RB convection [95].

3.1.2. The TLC technique.   Here, the key idea of the TLC technique is that the peak wavelength of the scattered light of TLC microspheres changes with fluid temperature. Usually, the TLC microspheres are neutrally buoyant and hence can be used as passive tracers. Figure 23 shows a schematic diagram of the optical setup for the TLC visualization. A halogen photo optic lamp (S) is used as the source of white light. A concave mirror L1 and several condensing lenses (L2 and L3) are used to collect the light from S and focus it onto the central section of the cell. A sheet of light, generated by a diverging cylindrical lens L4 and then projected onto an adjustable slit, is passed through the cell. In the figure, a horizontal light sheet is generated [88] to visualize the horizontal flow near the top plate. By adjusting the position and orientation of the slit, one can also generate other kinds of light sheets, like a vertical sheet [87, 98]. A CCD camera is used to take streak photographs of the TLC microspheres. With short camera exposure time the photographs give the instantaneous temperature field, and with long exposure time they will in addition show the trajectories of the particles.

Using the TLC technique, Zhou *et al* [88] revealed how sheetlike plumes evolute morphologically to mushroomlike ones near the plates. As shown in the left panel of figure 24, the motion of TLC microspheres appears to emanate from certain regions or 'sources' with bluish colour, suggesting that hot fluid (plumes) moves upwards, impinging on and spreading horizontally along the top plate. Along the particle traces, the colour turns from blue to green and red, implying that the wave fronts are cooled down gradually by the top plate (and the top thermal boundary layer) as they spread. As they travel along the plate surface, sheetlike plumes collide with each other or with the sidewall. As different plumes carry momentum in different directions, they merge, convolute and form swirls (hence generating vorticity). As these swirls are cooler than the bulk fluid, they spiral away from the plate, and then merge and cluster together.

Based on the TLC technique, Zhou and Xia [97] further developed a tomographic reconstruction technique to construct the 3D image of thermal plumes from sequences of 2D images acquired near the top plate of the cell. They placed the convection cell on a translational stage. The cell traversed continuously, during which a series of photographs of TLC microspheres were recorded by a colour camera. In post-experiment analysis, 2D
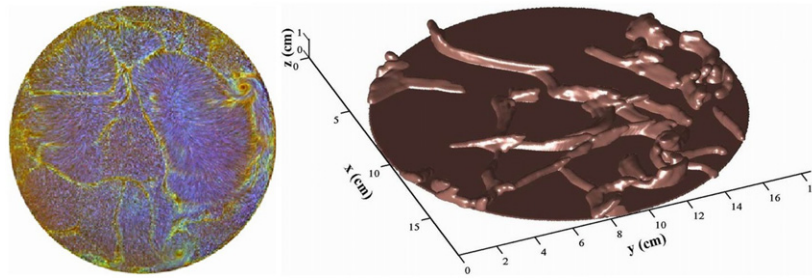
Figure 24. Left: reproduced with permission from [88]. Copyright 2007 by the American Physical Society. A image of TLC microspheres taken at 2 mm from the top plate in a water-filled $\Gamma = 1$ cylindrical cell with height 18.5 cm. The used particles have a mean diameter of 50 μm and density of 1.03–1.05 g cm^{-3}, and were suspended in the convecting fluid in very low concentrations (0.01 wt%). The peak wavelength of their scattered light changes within a temperature window divided as follows: 29°–29.5° for red, 29.5°–29.7° for green, and 29.7°–33° for blue. The camera exposure time is 0.77 s. Right: figure taken from [97]. Three-dimensional thermal plumes obtained near the top plate using the TLC tomographic reconstruction technique. Both measurements were made at $Ra = 2.0 \times 10^9$ and $Pr = 5.4$ in a $\Gamma = 1$ cell.
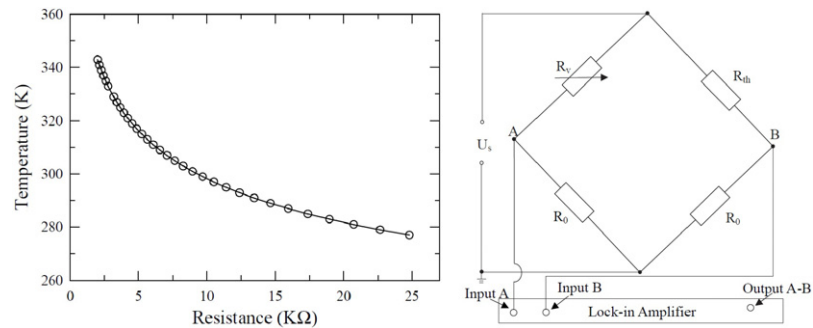

Figure 25. Figure reproduced from [99]. Left panel: a typical relationship curve for thermistor: temperature versus resistance. Right panel: the Wheatstone bridge. R_v is used to balance the bridge.

horizontal cuts of cold plumes were extracted from the images taken in each run and a MATLAB script was used to reconstruct 3D thermal plumes from these extracted 2D cuts. The right panel of figure 24 shows an example of the reconstruction of 3D thermal plumes near the top plate. One noteworthy feature is that most plumes have a 1D structure, rather than a sheetlike shape: both the height and the width of this plume extend only to a few millimetres, while its length extends to a few centimetres. Based on this, Zhou and Xia [97] suggest that the so-called sheetlike plumes are really 1D structures and may be called rodlike plumes.

3.2. Temperature measurements

Temperature measurement is surely essential for thermal turbulence. Usually, a temperature sensitive resistor, like a thermistor, is used as a thermal probe. Most thermistors have a negative temperature coefficient, i.e. their resistance decreases with increasing temperature. A slight temperature change causes a rapid and pronounced change in electrical resistance. As shown in the left panel of figure 25, the relationship between absolute temperature T (in Kelvins)
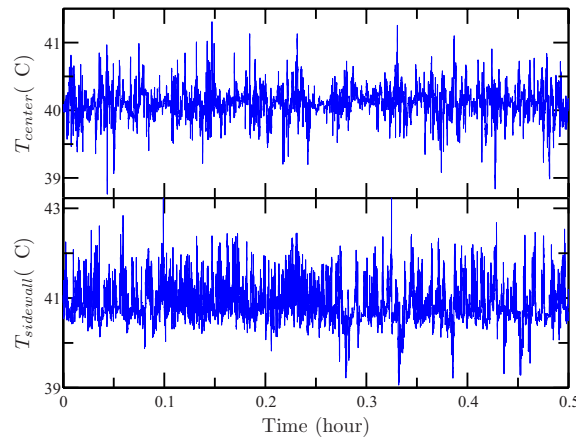
Figure 26. Temperature time series in the working fluid of water at the cell centre and near the sidewall at $Ra = 1 \times 10^{10}$ and $Pr = 4.3$.

and thermistor resistance R is well described by the equation proposed by Steinhart and Hart [100]:

$$\frac{1}{T} = a_0 + a_1(\ln R) + a_2(\ln R)^3, \tag{21}$$

where a_0, a_1, and a_2 are the fitting parameters. (The most general form of the applied equation contains a $(\ln R)^2$ term, but this is frequently neglected because it is typically much smaller than the other terms.) Thermistors are usually used to monitor the temperatures of the top and the bottom plates, as well as local temperatures in the cell, such as those within the thermal boundary layers [101, 102]. Fast and accurate measurement of the thermistor resistance gives us a direct reading of the precise local temperature fluctuations. To achieve this, a Wheatstone bridge is usually adopted. The right panel of figure 25 shows the circuit of an ac Wheatstone bridge. Ac source is often chosen rather than dc source for better sensitivity, more accuracy and less noise. Two arms of the bridge are precision resistors of resistance R_0. A variable resistor R_v and the thermistor R_{th} are connected to the other two arms. The ac source (U_s) supplied to the bridge is a sinusoidal wave with frequency much higher than sampling frequency. For a given value of the variable resistance R_v, the thermistor resistance R_{th} can be calculated from the following equation:

$$R_{th} = \frac{R_0}{\frac{R_0}{R_0 + R_v} - \frac{U_{AB}}{U_s}} - R_0, \tag{22}$$

where U_{AB} is the voltage difference between points A and B. A lock-in amplifier is used to measure this voltage difference. Figure 26 shows an example of the temperature time series measured with a thermistor in the working fluid of water at the cell centre and near the sidewall at $Ra = 1 \times 10^{10}$ and $Pr = 4.3$. One can clearly see that the measurements can well resolve small amplitude fluctuations.

3.3. Velocity measurements

The conventional velocimetry techniques, such as hot-wire or hot-film anemometers, have been widely used to measure the velocity in various turbulent flows as discussed above. However, these techniques are usually operated with a constant-temperature circuit and hence they are
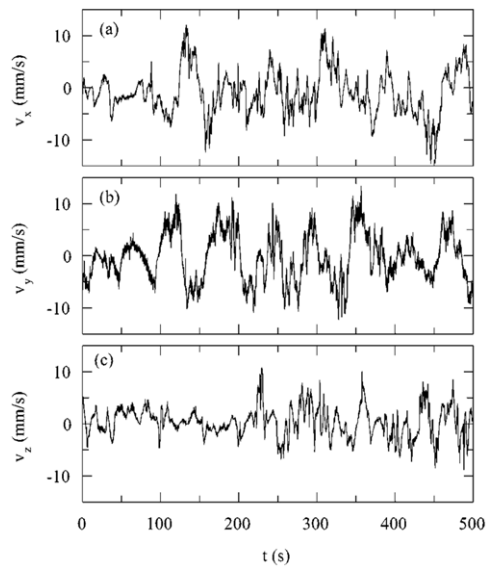
Figure 27. Figure reprinted with permission from [110]. Copyright 2004, AIP Publishing LLC. The measured time series of velocity fluctuations at the cell centre measured with LDA. The measurements are made at $Ra = 3.7 \times 10^9$ and the three velocity components are (*a*) v_x, (*b*) v_y and (*c*) v_z.

not ideal for use in thermal turbulence, like turbulent RB convection. On the other hand, optical techniques have developed greatly in the past several decades in the application of fluid flows because they can provide an insight into the flow structure. Combined with quantitative measurements of specific flow parameters such as velocity, density, pressure and temperature, they provide an accurate and complete picture of the flow. In this section, we discuss the applications of two popular optical velocimetry techniques in turbulent RB convection, i.e. LDA and PIV.

3.3.1. Laser Doppler anemometry.   The principle of LDA has already been discussed above, and it is widely used to measure the velocity fluctuations in turbulent flows. In the past decade, LDA has been widely used in turbulent RB systems, see, e.g. experiments by Ashkenazi and Steinberg [103], Daya and Ecke [104], Qiu and Tong [105, 106], Shang and Xia [107] and Du Puits *et al* [108, 109] among others. Figure 27 shows an example of the time series of velocity fluctuations at the cell centre measured with LDA [110]. The fluctuations of the velocity are nicely quantified with this technique.

3.3.2. Particle image velocimetry.   The technique of PIV provides us with a convenient tool to directly visualize and measure the flow field of a particular plane of interest in three-dimensional turbulent systems [112]. The details of the PIV technique have already been discussed above. With the PIV technique one captures two consecutive two-dimensional (2D) images of the seed particles, using a CCD camera situated normal to an illuminating light sheet as shown in figure 28. Spatial correlations between the two images are then calculated to obtain information about the displacement of the particles, from which one obtains the velocity map. The main advantage of the PIV method is its ability to follow the motion of a 2D flow field. With the 2D time series data, one can obtain both the time-averaged and the dynamic
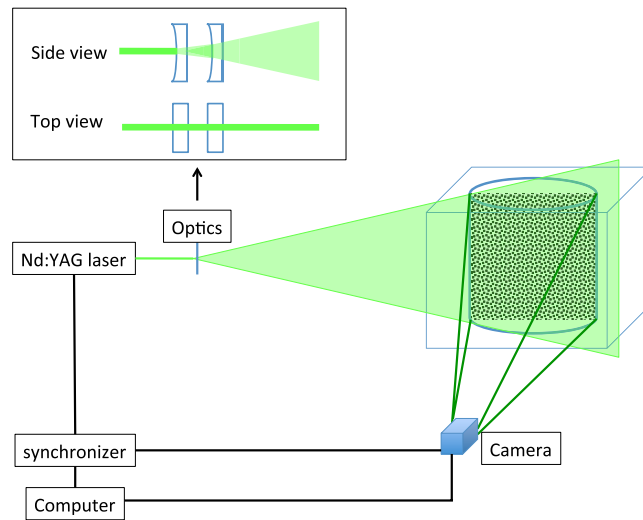
Figure 28. Sketch of the setup for PIV measurement for a cylindrical RB cell. The PIV system consists of a dual neodymium-doped yttrium aluminum garnet (Nd : YAG) laser, lightsheet optics, a cooled CCD camera, and a synchronizer.
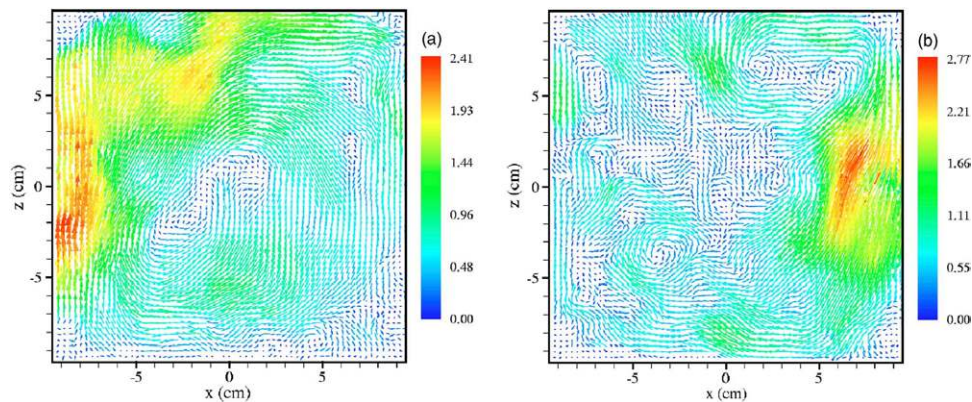

Figure 29. Figure reproduced with permission from [111]. Copyright 2005 by the American Physical Society. Instantaneous velocity vector maps taken in the plane of the LSC at $Ra = 7.0 \times 10^9$. The magnitude of the velocity is coded in colour and the length of the arrows in units of cm s^{-1}. Instantaneous velocity map taken at (*a*) early time and (*b*) 20 s (about half of the oscillation period at this Ra) later.

properties of the 2D flow field. By measuring the velocity maps in different planes, one can examine the 3D structures and dynamics of the velocity field. The light sheet is generated using cylindrical lenses as indicated in the inset of the figure 28. A square-shaped jacket made of flat glass plate is fitted to the outside of the sidewall. The jacket is also filled with water, which greatly reduces the distortion effect to the PIV images caused by the curvature of the cylindrical sidewall [111]. Instantaneous image capture and high spatial resolution of the PIV allow the detection of spatial structures even in unsteady flow fields, see Sun *et al* [111, 113]. Figure 29 shows two examples of the instantaneous velocity maps, which reveal the spatial coherence of the thermal plumes and bulk velocity oscillation (see [111] for further details).
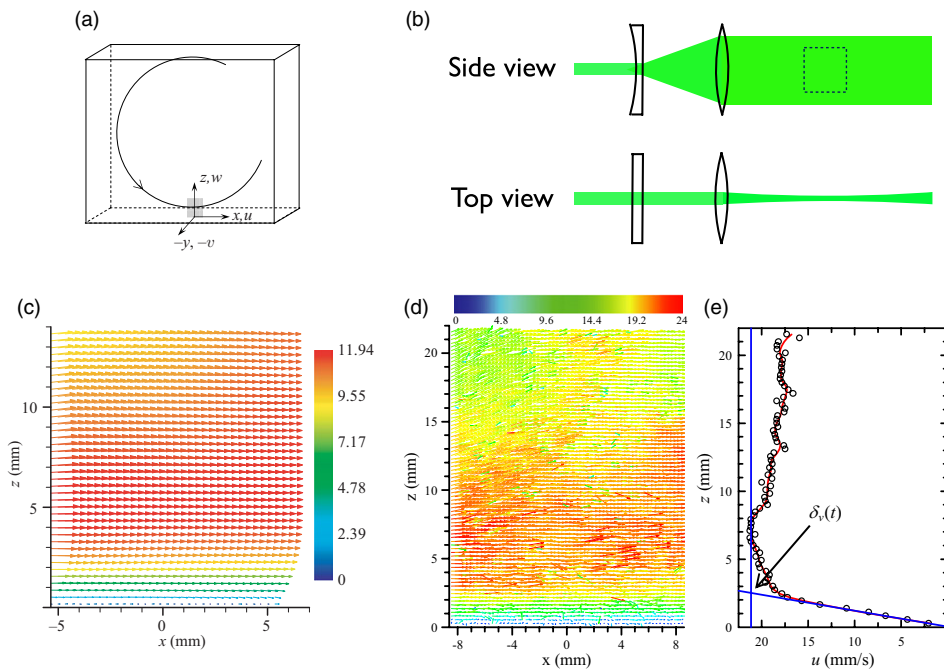
Figure 30. (*a*) and (*c*) Reproduced with permission from [114]. (*a*) Sketch of the convection cell and the Cartesian coordinates used in velocity measurements. The shaded region represents the PIV measuring area (11.07 mm × 13.84 mm). (*b*) The optics for the thin light sheet generation for the boundary layer measurements. (*c*) Coarse-grained vector maps of the time-averaged velocity field measured near the centre of the bottom plate ($Ra = 5.3 \times 10^9$). The unit is mm s^{-1}. (*d*), (*e*) Figure taken from [115]. An example of the instantaneous velocity field and the horizontal velocity profile measured near the centre of the bottom plate ($Ra = 1.9 \times 10^{11}$). The solid lines illustrate how the instantaneous viscous boundary layer thickness is obtained.

Recently, a high-resolution PIV technique has been employed to study the viscous boundary layer structures in turbulent RB convection [114, 115], as shown in figures 30(*a*)–(*c*). A very small area (shaded region in (*a*)) is illuminated with a thin light sheet (∼0.2 mm) generated with the optics shown in figure 30(*b*). The time-averaged and instantaneous velocity maps at two different Ra numbers are shown in figures 30(*c*) and (*d*), respectively. Sun *et al* [114] found that, despite the intermittent emission of plumes, the Prandtl–Blasius-type laminar boundary layer description is indeed a good approximation, in a time-averaged sense, both in terms of its scaling and its various dynamical properties. Zhou and Xia [115] further showed that the velocity profiles agree well with the classical Prandtl–Blasius laminar boundary-layer profile, if they are resampled in the dynamical reference frames that fluctuate with the instantaneous velocity boundary-layer thickness as shown in figures 30(*d*) and (*e*).

3.4. Global heat transport and local heat flux

The global heat transport can be measured by monitoring the input heat-current from bottom plate. The main challenge is to reduce the heat leakage from the sidewall and bottom plate. Brown *et al* [116] provided detailed descriptions on the construction of the system to minimize the heat leakage. We refer the reader to [116] for more details on the global heat transport
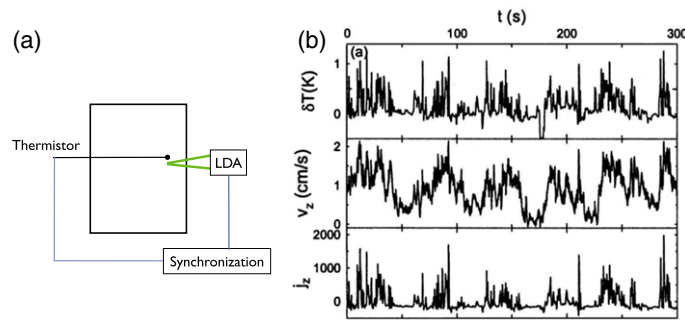
Figure 31. Reproduced with permission from [60]. Copyright 2003 by the American Physical Society. (*a*) A schematic drawing illustrating the simultaneous measurements of velocity and temperature. (*b*) Time series of the temperature fluctuation $\delta T(t)$ (top curve), vertical velocity (middle curve) $v_z(t)$, and instantaneous vertical flux $J_z(t)$ (bottom curve) near the sidewall. The measurements were made at $Ra = 3.6 \times 10^9$.

measurements. Many experiments on the global measurements of the Nusselt number were conducted with wide parameter range and great precision, see recent review articles by Ahlers *et al* [14], by Chillà and Schumacher [117] and by Xia [118] for further details.

Shang *et al* [60, 119, 120] directly measured the local convective heat flux, $J(r, t) = \langle v(r, t)\delta T(r, t)\rangle_t H/\kappa\Delta$, at different Ra and spatial positions (r). Here, $\langle\ldots\rangle_t$ indicates an average over time t. To obtain the local heat flux, one has to measure the local temperature fluctuation $\delta T = T(r, t) - T_0$ and local flow velocity $v(r, t)$ at the same position simultaneously (here T_0 is the mean bulk temperature). As shown in figure 31, a small movable thermistor of 0.2 mm in diameter, 15 ms in time constant, was used to measure $T(r, t)$. The local velocity was measured using a LDA. Simultaneous velocity and temperature measurements were realized using a multichannel LDA interface module to synchronize the data acquisition. A triggering pulse from the LDA signal processor initiated the acquisition of an analogue temperature signal. Figure 31(*b*) shows the measured time series of the temperature fluctuation $\delta T(t)$ (top curve), vertical velocity (middle curve) $v_z(t)$, and the instantaneous vertical flux $J_z(t)$ (bottom curve) near the sidewall. The local heat flux was measured with very good precision, and the measured results are nicely consistent with the theoretical predictions [5] and recent numerical simulations [121]. Recently, by using commercial heat flux sensors, du Puits *et al* [122] measured the local heat flux simultaneously at the surfaces of the heating and the cooling plates (see [122] for further details).

4. Summary

In this paper, we have reviewed the various experimental techniques that have been used to study closed turbulent flow systems, with the example of two well-known systems: turbulent Taylor–Couette (TC) flow and turbulent Rayleigh–Bénard (RB) convection. In TC flow, we mainly focus on the measurement techniques of the flow structures, the angular velocity of the flow (transport quantity), the radial velocity (wind velocity), the global torque, and the local turbulent angular velocity flux. In RB convection, we focus on the techniques used to measure the flow structures, the temperature and velocity of the fluid, and the global and local heat flux. There have also been many new developments of the measurement techniques for RB and TC systems in recent years, like 3D-PTV for RB [123], the instrumented tracer for

Lagrangian measurements in RB [124, 125], the measurement technique for the effective wind Reynolds number for RB [126], and the high-resolution PIV measurement technique for TC boundary layers [127], etc. These developments are beyond the scope of the present paper. New emerging technologies will certainly provide better experimental techniques for both turbulent TC flow and RB turbulence in future.

Acknowledgments

References

[1] Lathrop D P, Fineberg J and Swinney H L 1992 Transition to shear-driven turbulence in Couette–Taylor flow *Phys. Rev.* A **46** 6390
[2] Eckhardt B, Grossmann S and Lohse D 2007 Torque scaling in turbulent Taylor–Couette flow between independently rotating cylinders *J. Fluid Mech.* **581** 221
[3] Grossmann S and Lohse D 2000 Scaling in thermal convection: a unifying view *J. Fluid. Mech.* **407** 27
[4] Grossmann S and Lohse D 2001 Thermal convection for large Prandtl number *Phys. Rev. Lett.* **86** 3316
[5] Grossmann S and Lohse D 2004 Fluctuations in turbulent Rayleigh–Bénard convection: the role of plumes *Phys. Fluids* **16** 4462
[6] Taylor G I 1923 Stability of a viscous liquid contained between two rotating cylinders *Phil. Trans. R. Soc. Lond.* A **223** 289
[7] DiPrima R C and Swinney H L 1981 Instabilities and transition in flow between concentric rotating cylinders *Hydrodynamic Instabilities and the Transition to Turbulence* ed H L Swinney and J P Gollub (Berlin: Springer)
[8] Andereck C D, Liu S S and Swinney H L 1986 Flow regimes in a circular Couette system with independently rotating cylinders *J. Fluid Mech.* **164** 155
[9] Mullin T, Cliffe K A and Pfister G 1987 Unusual time-dependent phenomena in Taylor–Couette flow at moderately low Reynolds-numbers *Phys. Rev. Lett.* **58** 2212
[10] Dominguez-Lerma M A, Cannell D S and Ahlers G 1986 Eckhaus boundary and wave-number selection in rotating Couette–Taylor flow *Phys. Rev.* A **34** 4956
[11] Ning L, Ahlers G and Cannell D S 1990 Wave-number selection and traveling vortex waves in spatially ramped Taylor–Couette flow *Phys. Rev. Lett.* **64** 1235
[12] Babcock K L, Ahlers G and Cannell D S 1991 Noise-sustained structure in Taylor–Couette flow with through flow *Phys. Rev. Lett.* **67** 3388
[13] Bodenschatz E, Pesch W and Ahlers G 2000 Recent developments in Rayleigh–Bénard convection *Annu. Rev. Fluid Mech.* **32** 709
[14] Ahlers G, Grossmann S and Lohse D 2009 Heat transfer and large scale dynamics in turbulent Rayleigh–Bénard convection *Rev. Mod. Phys.* **81** 503

[15] Lohse D and Xia K-Q 2010 Small-scale properties of turbulent Rayleigh–Bénard convection *Annu. Rev. Fluid Mech.* **42** 335

[16] Matisse P and Gorman M 1984 Neutrally buoyant anisotropic particles for flow visualization *Phys. Fluids* **27** 759

[17] Gorman M and Swinney H L 1982 Spatial and temporal characteristics of modulated waves in the circular Couette system *J. Fluid Mech.* **117** 123

[18] Borrero-Echeverry D, Schatz M F and Tagg R 2010 Transient turbulence in Taylor–Couette flow *Phys. Rev.* E **81** 025301

[19] van Gils D P M, Huisman, Sun C and Lohse D 2013 unpublished

[20] van Gils D P M, Bruggert G W, Lathrop D P, Sun C and Lohse D 2011 The Twente turbulent Taylor–Couette (T^{3}C) facility: strongly turbulent (multiphase) flow between two independently-rotating cylinders *Rev. Sci. Instrum.* **82** 025105

[21] Toschi F and Bodenschatz E 2009 Lagrangian properties of particles in turbulence *Annu. Rev. Fluid Mech.* **41** 375

[22] Tagawa Y, Martinez J, Prakash V N, Calzavarini E, Sun C and Lohse D 2012 Three-dimensional Lagrangian Voronoi analysis for clustering of particles and bubbles in turbulence *J. Fluid Mech.* **693** 201

[23] Calzavarini E, Kerscher M, Lohse D and Toschi F 2008 Dimensionality and morphology of particle and bubble clusters in turbulent flow *J. Fluid Mech.* **607** 13

[24] Sugiyama K, Calzavarini E and Lohse D 2008 Microbubble drag reduction in Taylor–Couette flow in the wavy vortex regime *J. Fluid Mech.* **608** 21

[25] Tropea C, Yarin A L and Foss J F 2007 *Handbook of Experimental Fluid Mechanics* (Berlin: Springer)

[26] Lewis G S 1996 *PhD Thesis* University of Texas at Austin

[27] Smith G P and Townsend A A 1982 Turbulent Couette flow between concentric cylinders at large Taylor numbers *J. Fluid Mech.* **123** 187

[28] van Gils D P M, Huisman S G, Grossmann S, Sun C and Lohse D 2012 Optimal Taylor–Couette turbulence *J. Fluid Mech.* **708** 118

[29] Wendt F 1933 Turbulente Strömungen zwischen zwei rotierenden konaxialen Zylindern *Arch. Appl. Mech.* **4** 577

[30] Lewis G S and Swinney H L 1999 Velocity structure functions, scaling, and transitions in high-Reynolds-number Couette–Taylor flow *Phys. Rev.* E **59** 5457

[31] Dantec, Inc. Probes for Hot-wire Anemometry, Dantec Dynamics A/S, Denmark

[32] Martinez J, Prakash V N, Tagawa Y, Sun C and Lohse D 2012 Lagrangian statistics of light particles in turbulence *Phys. Fluids* **24** 055106

[33] Coles D and Van Atta C 1966 Measured distortion of a laminar circular Couette flow by end effects *J. Fluid Mech.* **25** 513

[34] Martinez-Mercado J, Palacios-Morales C A and Zenit R 2007 Measurement of pseudoturbulence intensity in monodispersed bubbly liquids for $10 < Re < 500$ *Phys. Fluids* **19** 103302

[35] Wallace J M and Vukoslavčević P V 2010 Measurement of the velocity gradient tensor in turbulent flows *Annu. Rev. Fluid Mech.* **42** 157

[36] Sun C, Mullin T, van Wijngaarden L and Lohse D 2010 Drag and lift forces on a counter-rotating cylinder in rotating shear flow *J. Fluid Mech.* **664** 150

[37] Albrecht H-E, Borys M, Damaschke N and Tropea C 2003 *Laser Doppler and Phase Doppler Measurements Techniques* (Berlin: Springer)

[38] Maas H G, Gruen A and Papantoniou D 1993 Particle tracking velocimetry in three-dimensional flows *Exp. Fluids* **15** 133

[39] Ouellette N, Xu H and Bodenschatz E 2006 A quantitative study of three-dimensional Lagrangian particle tracking algorithms *Exp. Fluids* **40** 301

[40] Raffel M, Willert C, Wereley S and Kompenhans J 2007 *Partical Image Velocimetry: A Practical Guide* (Berlin: Springer)

[41] Ravelet F, Delfos R and Westerweel J 2010 Influence of global rotation and Reynolds number on the large-scale features of a turbulent Taylor–Couette flow *Phys. Fluids* **22** 055103

[42] Dantec 2010 *Dantec Reference manual: FiberFlow. Installation & User's guide* (Dantec Measurement Technology, Denmark)

[43] Dantec 2010 *Dantec Reference manual: Burst Spectrum Analyzer. Installation & User's guide* (Dantec Measurement Technology, Denmark)

[44] Buchhave P, George W K and Lumley J L 1979 The measurement of turbulence with the laser–Doppler anemometer *Annu. Rev. Fluid Mech.* **11** 443

[45] Huisman S, van Gils D and Sun C 2012 Applying laser Doppler anemometry inside a Taylor–Couette geometry using a ray-tracer to correct for curvature effects *Euro. J. Mech.* B **36** 115

[46] Zhang Z 2004 Optical guidelines and signal quality for LDA applications in circular pipes *Exp. Fluids* **37** 29

[47] Adrian R J and Westerweel J 2010 *Particle Image Velocimetry* (Cambridge: Cambridge University Press)

[48] Raffel M, Willert C E, Wereley S T and Kompenhans J 2007 *Particle Image Velocimetry: A Practical Guide* (Berlin: Springer)

[49] Huisman S, Sun C and Lohse D 2013 unpublished

[50] Sun C, Xi H-D and Xia K-Q 2006 Azimuthal symmetry, flow dynamics, and heat transport in turbulent thermal convection in a cylinder with an aspect ratio of 0.5 *Phys. Rev. Lett.* **95** 074502

[51] Tong P, Goldburg W I, Huang J S and Witten T A 1990 Anisotropy in turbulent drag reduction *Phys. Rev. Lett.* **65** 2780

[52] Lathrop D P, Fineberg J and Swinney H L 1992 Turbulent flow between concentric rotating cylinders at large Reynolds numbers *Phys. Rev. Lett.* **68** 1515

[53] Narezo-Guzman D 2011 Bubble deformability is crucial for strong drag reduction in bubbly turbulent Taylor–Couette flow *Master's Thesis* University of Twente

[54] van Gils D P M, Huisman S G, Bruggert G, Sun C and Lohse D 2011 Torque scaling in turbulent Taylor–Couette flow with co- and counterrotating cylinders *Phys. Rev. Lett.* **106** 024502

[55] Paoletti M S and Lathrop D P 2011 Angular momentum transport in turbulent flow between independently rotating cylinders *Phys. Rev. Lett.* **106** 024501

[56] Merbold S, Brauckmann H J and Egbers C 2013 Torque measurements and numerical determination in differentially rotating wide gap Taylor–Couette flow *Phys. Rev.* E **87** 023014

[57] Ji H, Burin M, Schartman E and Goodman J 2006 Hydrodynamic turbulence cannot transport angular momentum effectively in astrophysical disks *Nature* **444** 343

[58] Burin M J, Schartman E and Ji H 2010 Local measurements of turbulent angular momentum transport in circular Couette flow *Exp. Fluids* **48** 763

[59] Huisman S G, van Gils D P M, Grossmann S, Sun C and Lohse D 2012 Ultimate turbulent Taylor–Couette flow *Phys. Rev. Lett.* **108** 024501

[60] Shang X D, Qiu X L, Tong P and Xia K-Q 2003 Measured local heat transport in turbulent Rayleigh–Bénard convection *Phys. Rev. Lett.* **90** 074501

[61] Ceccio S L 2010 Friction drag reduction of external flows with bubble and gas injection *Annu. Rev. Fluid Mech.* **42** 183

[62] Djeridi H, Gabillet C and Billard J Y 2004 Two-phase Couette–Taylor flow: arrangement of the dispersed phase and effects on the flow structures *Phys. Fluids* **16** 128

[63] van den Berg T H, Luther S, Lathrop D P and Lohse D 2005 Drag reduction in bubbly Taylor–Couette turbulence *Phys. Rev. Lett.* **94** 044501

[64] Murai Y, Oiwa H and Takeda Y 2005 Bubble behavior in a vertical Taylor–Couette flow *J. Phys.: Conf. Ser.* **14** 143

[65] van den Berg T H, van Gils D P M, Lathrop D P and Lohse D 2007 Bubbly turbulent drag reduction is a boundary layer effect *Phys. Rev. Lett.* **98** 084501

[66] Prakash V N, Tagawa Y, Calzavarini E, Martinez J, Toschi F, Lohse D and Sun C 2012 How gravity and size affect the acceleration statistics of bubbles in turbulence *New J. Phys.* **14** 105017

[67] Mudde R F and Saito T 2001 Hydrodynamical similarities between bubble column and bubbly pipe flow *J. Fluid Mech.* **437** 203

[68] Xue J, Al-Dahhan M, Dudokovic M P and Mudde R F 2003 Bubble dynamics measurements using four-point optical probe *Can. J. Chem. Eng.* **81** 375

[69] Guet S, Fortunati R V, Mudde R F and Ooms G 2003 Bubble velocity and size measurement with a four-point optical fiber probe *Part. Part. Syst. Charact.* **20** 219

[70] Luther S, Rensen J and Guet S 2004 Bubble aspect ratio and velocity measurement using a four-point fiber-optical probe *Exp. Fluids* **36** 326

[71] Wu C, Suddard K and Al-dahhan M H 2008 Bubble dynamics investigation in a slurry bubble column *AIChE J.* **54** 1203

[72] Xue J, Al-Dahhan M, Dudukovic M P and Mudde R F 2008 Four-point optical probe for measurement of bubble dynamics: validation of the technique *Flow Meas. Instrum.* **19** 293

[73] Martinez J, Chehata D, Gils D, Sun C and Lohse D 2010 On bubble clustering and energy spectra in pseudo-turbulence *J. Fluid Mech.* **650** 287

[74] van den Berg T H, Wormgoor W D, Luther S and Lohse D 2011 Phase sensitive constant temperature anemometry *Macromol. Mater. Eng.* **296** 230

[75] Cartellier A and Achard J L 1991 Local phase detection probes in fluid/fluid two-phase flows *Rev. Sci. Instrum.* **62** 279

[76] van Gils D P M, Narezo Guzman D, Sun C and Lohse D 2013 The importance of bubble deformability for strong drag reduction in bubbly turbulent Taylor–Couette flow *J. Fluid Mech.* **722** 317

[77] Krishnamurti R and Howard L N 1981 Large-scale flow generation in turbulent convection *Proc. Natl Acad. Sci. USA* **78** 1981

[78] Haramina T and Tilgner A 2004 Coherent structures in boundary layers of Rayleigh–Bénard convection *Phys. Rev.* E **69** 056306

[79] Puthenveettil B and Arakeri J 2005 Plume structure in high-Rayleigh-number convection *J. Fluid Mech.* **542** 217

[80] Zhou Q and Xia K-Q 2010 The mixing evolution and geometric properties of a passive scalar field in turbulent Rayleigh–Bénard convection *New J. Phys.* **12** 083029

[81] Zhang J, Childress S and Libchaber A 1997 Non-Boussinesq effect: thermal convection with broken symmetry *Phys. Fluids* **9** 1034

[82] Trainoff S P and Cannell D S 2002 Physical optics treatment of the shadowgraph *Phys. Fluids* **14** 1340

[83] Xi H-D, Lam S and Xia K-Q 2004 From laminar plumes to organized flows: the onset of large-scale circulation in turbulent thermal convection *J. Fluid Mech.* **503** 47

[84] Bosbach J, Weiss S and Ahlers G 2012 Plume fragmentation by bulk interactions in turbulent Rayleigh–Bénard convection *Phys. Rev. Lett.* **108** 054501

[85] Zocchi G, Moses E and Libchaber A 1990 Coherent structures in turbulent convection, an experimental study *Physica* A **166** 387

[86] Gluckman B J, Willaime H and Gollub J P 1993 Geometry of isothermal and isoconcentration surface in thermal turbulence *Phys. Fluids* A **5** 647

[87] Du Y-B and Tong P 1998 Enhanced heat transport in turbulent convection over a rough surface *Phys. Rev. Lett.* **81** 987

[88] Zhou Q, Sun C and Xia K-Q 2007 Morphological evolution of thermal plumes in turbulent Rayleigh–Bénard convection *Phys. Rev. Lett.* **98** 074501

[89] Shang X-D, Qiu X-L, Tong P and Xia K-Q 2003 Measured local heat transport in turbulent Rayleigh–Bénard convection *Phys. Rev. Lett.* **90** 074501

[90] Xi H-D and Xia K-Q 2008 Azimuthal motion, reorientation, cessation, and reversal of the large-scale circulation in turbulent thermal convection: a comparative study in aspect ratio one and one-half geometries *Phys. Rev.* E **78** 036326

[91] Funfschilling D and Ahlers G 2004 Plume motion and large-scale circulation in a cylindrical Rayleigh–Bénard cell *Phys. Rev. Lett.* **92** 194502

[92] Funfschilling D, Brown E and Ahlers G 2008 Azimuthal oscillations of the large-scale circulation in turbulent Rayleigh–Bénard convection *J. Fluid Mech.* **607** 119

[93] Funfschilling D and Ahlers G 2004 Plume motion and large scale circulation in a cylindrical Rayleigh–Bénard cell *Phys. Rev. Lett.* **92** 194502

[94] Bosbach J, Weiss S and Ahlers G 2012 Plume fragmentation by bulk interactions in turbulent Rayleigh–Bénard convection *Phys. Rev. Lett.* **108** 054501

[95] Zhong J-Q, Funfschilling D and Ahlers G 2009 Enhanced heat transport by turbulent two-phase Rayleigh–Bénard convection *Phys. Rev. Lett.* **102** 124501

[96] de Bruyn J R, Bodenschatz E, Morris S W, Trainoff S P, Hu Y, Cannell D S and Ahlers G 1996 Apparatus for the study of Rayleigh–Bénard convection in gases under pressure *Rev. Sci. Instrum.* **67** 2043

[97] Zhou Q and Xia K-Q 2010 Physical and geometrical properties of thermal plumes in turbulent Rayleigh–Bénard convection *New J. Phys.* **12** 075006

[98] Du Y-B and Tong P 2000 Turbulent thermal convection in a cell with ordered rough boundaries *J. Fluid Mech.* **407** 57

[99] Zhou Q 2005 Experimental investigation of scalar mixing and self-organized structures in thermal turbulence *Master's Thesis* the Chinese University of Hong Kong

[100] Steinhart J S and Hart S R 1968 Calibration curves for thermistors *Deep Sea Res. Oceanogr. Abstr.* **15** 497

[101] du Puits R, Resagk C and Thess A 2013 Thermal boundary layers in turbulnet Rayleigh–Bénard convection at aspect ratios between 1 and 9 *New J. Phys.* **15** 013040

[102] Zhou Q and Xia K-Q 2013 Thermal boundary layer structure in turbulent Rayleigh–Bénard convection in a rectangular cell *J. Fluid Mech.* **721** 199

[103] Ashkenazi S and Steinberg V 1999 Spectra and statistics of velocity and temperature fluctuations in turbulent convection *Phys. Rev. Lett.* **83** 4760

[104] Daya Z A and Ecke R E 2001 Does turbulent convection feel the shape of the container? *Phys. Rev. Lett.* **87** 184501

[105] Qiu X-L, Yao S H and Tong P 2000 Large-scale coherent rotation and oscillation in turbulent thermal convection *Phys. Rev.* E **61** R6075

[106] Qiu X-L and Tong P 2001 Large-scale velocity structures in turbulent thermal convection *Phys. Rev.* E **64** 036304

[107] Shang X-D and Xia K-Q 2001 Scaling of the velocity power spectra in turbulent thermal convection *Phys. Rev.* E **64** 065301(R)

[108] du Puits R, Resagk C and Thess A 2007 Mean velocity profile in confined turbulent convection *Phys. Rev. Lett.* **99** 234504

[109] du Puits R, Resagk C and Thess A 2007 Breakdown of wind in turbulent thermal convection *Phys. Rev.* E **75** 016302

[110] Qiu X L, Shang X D, Tong P and Xia K-Q 2004 Velocity oscillations in turbulent Rayleigh–Bénard convection *Phys. Fluids* **16** 412

[111] Sun C, Xia K-Q and Tong P 2005 Three-dimensional flow structures and dynamics of turbulent thermal convection in a cylindrical cell *Phys. Rev.* E **72** 026302

[112] Adrian R J 1992 Particle-imaging techniques for experimental fluid-mechanics *Annu. Rev. Fluid Mech.* **23** 261

[113] Xia K-Q, Sun C and Zhou S-Q 2003 Particle image velocimetry measurement of the velocity field in turbulent thermal convection *Phys. Rev.* E **68** 066303

[114] Sun C, Cheung Y-H and Xia K-Q 2008 Experimental studies of the viscous boundary layer properties in turbulent Rayleigh–Bénard convection *J. Fluid Mech.* **79** 79

[115] Zhou Q and Xia K-Q 2010 Measured instantaneous viscous boundary layer in turbulent Rayleigh–Bénard convection *Phys. Rev. Lett.* **104** 104301

[116] Brown E, Funfschilling D, Nikolaenko A and Ahlers G 2005 Heat transport by turbulent Rayleigh–Bénard convection: effect of finite top- and bottom conductivity *Phys. Fluids* **17** 075108

[117] Chillà F and Schumacher J 2012 New perspectives in turbulent Rayleigh–Bénard convection *Eur. Phys. J.* E **35** 58

[118] Xia K-Q 2013 Current trends and future directions in turbulent thermal convection *Theor. Appl. Mech. Lett.* **3** 04200z

[119] Shang X-D, Qiu X-L, Tong P and Xia K-Q 2004 Measurements of the local convective heat flux in turbulent Rayleigh–Bénard convection *Phys. Rev.* E **70** 026308

[120] Shang X D, Tong P and Xia K-Q 2008 Scaling of the local convective heat flux in turbulent Rayleigh–Bénard convection *Phys. Rev. Lett.* **100** 244503

[121] Lakkaraju R, Stevens R J A M, Verzicco R, Grossmann S, Prosperetti A, Sun C and Lohse D 2012 Spatial distribution of heat flux and fluctuations in turbulent Rayleigh–Bénard convection *Phys. Rev.* E **86** 056315

[122] du Puits R, Resagk C and Thess A 2010 Measurements of the instantaneous local heat flux in turbulent Rayleigh–Bénard convection *New J. Phys.* **12** 075023

[123] Ni R, Huang S-D and Xia K-Q 2012 Lagrangian acceleration measurements in convective thermal turbulence *J. Fluid Mech.* **692** 395

[124] Shew W L, Gasteuil Y, Gibert M, Metz P and Pinton J-F 2007 Instrumented tracer for Lagrangian measurements in Rayleigh–Bénard convection *Rev. Sci. Instrum.* **78** 065105

[125] Gasteuil Y, Shew W L, Gibert M, Chillá F, Castaing B and Pinton J-F 2007 Lagrangian temperature, velocity, and local heat flux measurement in Rayleigh–Bénard convection *Phys. Rev. Lett.* **99** 234302

[126] He X, Funfschilling D, Nobach H, Bodenschatz E and Ahlers G 2012 Transition to the ultimate state of turbulent Rayleigh–Bénard convection *Phys. Rev. Lett.* **108** 024502

[127] Huisman S G, Scharnowski S, Cierpka C, Kähler C J, Lohse D and Sun C 2013 Logarithmic boundary layers in strong Taylor–Couette turbulence *Phys. Rev. Lett.* **110** 264501